Multi-Objective Flight Control for Drag Minimization and Load Alleviation of High-Aspect Ratio Flexible Wing Aircraft

Nhan Nguyen[*]

NASA Ames Research Center, Moffett Field, CA 94035

Eric Ting[†]

NASA Ames Research Center, Moffett Field, CA 94035

Daniel Chaparro[‡]

Stinger Ghaffarian Technologies, Inc., Moffett Field, CA 94035

Michael Drew[§]

Stinger Ghaffarian Technologies, Inc., Moffett Field, CA 94035

Sean Swei[¶]

NASA Ames Research Center, Moffett Field, CA 94035

As aircraft wings become much more flexible due to the use of light-weight composites material, adverse aerodynamics at off-design performance can result from changes in wing shapes due to aeroelastic deflections. Increased drag, hence increased fuel burn, is a potential consequence. Without means for aeroelastic compensation, the benefit of weight reduction from the use of light-weight material could be offset by less optimal aerodynamic performance at off-design flight conditions. Performance Adaptive Aeroelastic Wing (PAAW) technology can potentially address these technical challenges for future flexible wing transports. PAAW technology leverages multi-disciplinary solutions to maximize the aerodynamic performance payoff of future adaptive wing design, while addressing simultaneously operational constraints that can prevent the optimal aerodynamic performance from being realized. These operational constraints include reduced flutter margins, increased airframe responses to gust and maneuver loads, pilot handling qualities, and ride qualities. All of these constraints while seeking the optimal aerodynamic performance present themselves as a multi-objective flight control problem. The paper presents a multi-objective flight control approach based on a drag-cognizant optimal control method. A concept of virtual control, which was previously introduced, is implemented to address the pair-wise flap motion constraints imposed by the elastomer material. This method is shown to be able to satisfy the constraints. Real-time drag minimization control is considered to be an important consideration for PAAW technology. Drag minimization control has many technical challenges such as sensing and control. An initial outline of a real-time drag minimization control has already been developed and will be further investigated in the future. A simulation study of a multi-objective flight control for a flight path angle command with aeroelastic mode suppression and drag minimization demonstrates the effectiveness of the proposed solution. In-flight structural loads are also an important consideration. As wing flexibility increases, maneuver load and gust load responses can be significant and therefore can pose safety and flight control concerns. In this paper, we will extend the multi-objective flight control framework to include load alleviation control. The study will focus initially on maneuver load minimization control, and then subsequently will address gust load alleviation control in future work.

I. Introduction

Aircraft are typically designed to maintain efficient structural design for safe load-carrying capacity. Modern engineered materials such as composites have begun to appear in new airframe constructions for weight reduction

---

[*]Technical Group Lead and Research Scientist, Associate Fellow AIAA, Intelligent Systems Division, nhan.t.nguyen@nasa.gov

[†]Research Engineer, Intelligent Systems Division, eric.b.ting@nasa.gov

[‡]Research Engineer, Stinger Ghaffarian Technologies Inc., NASA Ames Research Center, daniel.chaparroespinoza@nasa.gov

[§]Research Engineer, Stinger Ghaffarian Technologies Inc., NASA Ames Research Center, michael.c.drew@nasa.gov

[¶]Research Scientist, Intelligent Systems Division, sean.s.swei@nasa.gov

American Institute of Aeronautics and Astronautics

purposes. A typical modern transport aircraft wing can provide less structural stiffness while maintaining the same load-carrying capacity as an older aluminum wing construction. There is a realization that next-generation aircraft concepts can be developed to take advantage of the structural flexibility afforded by modern engineered materials to improve the aerodynamic performance.

As aircraft wings become more flexible, adverse aerodynamics at off-design performance can result from changes in wing shapes due to aeroelastic deflections. Increased drag, hence increased fuel burn, is one such potential consequence. Without means for aeroelastic compensation, the benefit of weight reduction from the use of light-weight material could be offset by less optimal aerodynamic performance at off-design flight conditions. Performance Adaptive Aeroelastic Wing (PAAW) technology can potentially address these technical challenges for future flexible wing transports. PAAW technology leverages multi-disciplinary solutions to maximize the aerodynamic performance payoff of future adaptive wing design, while addressing simultaneously operational constraints that can prevent the optimal aerodynamic performance from being realized. These operational constraints include reduced flutter margins, increased airframe responses to gust and maneuver loads, and degraded pilot handling qualities as well as ride qualities. All of these constraints while seeking the optimal aerodynamic performance present themselves as a multi-objective flight control problem.

A multi-objective flight control framework has been developed to address these operational constraints and the efficiency goal simultaneously in order to arrive at optimal solutions that can provide good compromise between the efficiency goal and operational constraints. These optimal solutions take advantage of a multi-functional flight control system called the Variable Camber Continuous Trailing Edge Flap (VCCTEF) concept in this study. The VCCTEF is a possible candidate PAAW concept developed under the NASA Advanced Air Transport Technology (AATT) project.

The VCCTEF concept was originally developed by a NASA Innovation Fund study entitled "Elastically Shaped Future Air Vehicle Concept" in 2010.[1,2] This study examined new concepts that can enable active control of wing aeroelasticity to achieve drag reduction. The results showed that a highly flexible wing could be elastically shaped in-flight by active control of wing twist and vertical deflection in order to optimize the local angles of attack to improve the aerodynamic efficiency. The VCCTEF concept provides spanwise load tailoring via a continuous trailing edge formed by multiple spanwise flap sections which are joined together by elastomer transition sections as shown in Fig. 1. The spanwise load tailoring allows optimal lift distributions to be achieved throughout a given flight envelope, thereby enabling a mission-adaptive performance. A secondary benefit of the continuous trailing edge flap is the potential noise reduction during take-off and landing when the flap is configured for high-lift operations. In contrast, conventional flaps with gaps produce a significant noise source at high-lift conditions.
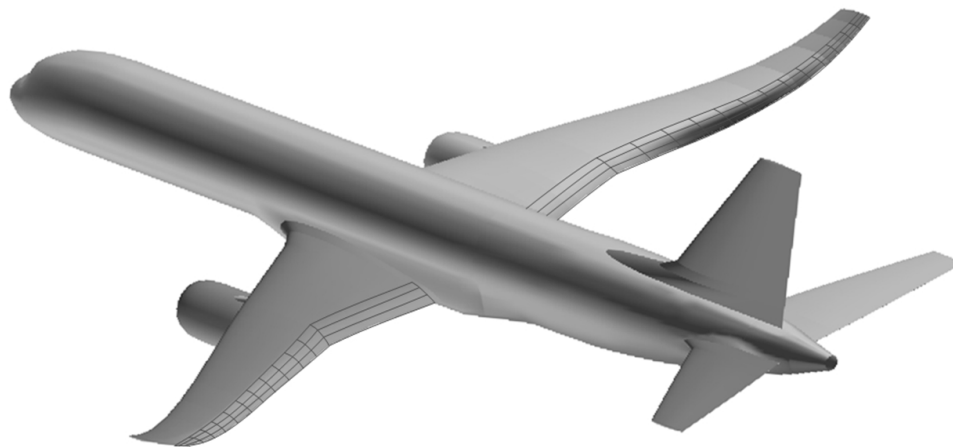
Figure 1. GTM with with Variable Camber Continuous Trailing Edge Flap

The VCCTEF also provides chordwise pressure shaping via a variable camber flap having three chordwise segments as shown in Fig. 2. These three chordwise flap segments can be individually commanded or actuated in unison when a flap deflection command is given. By varying the deflections of the individual chordwise flap segments, any camber surface can be created to achieve a desired aerodynamic performance. In general, a cambered flap is more efficient in producing lift than a straight conventional flap by achieving the same lift at a lower drag. The chordwise

American Institute of Aeronautics and Astronautics

pressure shaping modifies the pressure distribution on a wing surface to achieve a drag reduction or to reduce the shock formation on the wing's upper surface, thus allowing a higher cruise speed or reducing the transonic drag rise.

Initial study results indicate that the VCCTEF system can offer a potential pay-off in drag reduction that could translate into significant fuel savings. In order to realize the potential benefit of drag reduction by aeroelastic wing shaping control while meeting all other performance requirements and operational constraints, an integrated multidisciplinary approach is developed to incorporate a flight control system design into a modeling environment to maximize the system benefits of PAAW technology. Figure 1 illustrates the VCCTEF concept installed on a flexible wing GTM.
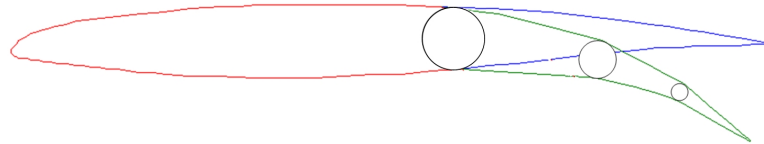

Figure 2. Three-Segment Variable Camber Flap

EQUAL CHORD **FLAP SECTIONS:**

• 24" TWIST SECTIONS WITH 8" SKIN   SEPARATOR SECTIONS
    • 13 x 24" WIDTH – ACTUATED TRI-FLAPS

• MAIN FLAP - 3 SECTIONS 75" WIDTH – *NO TWIST*
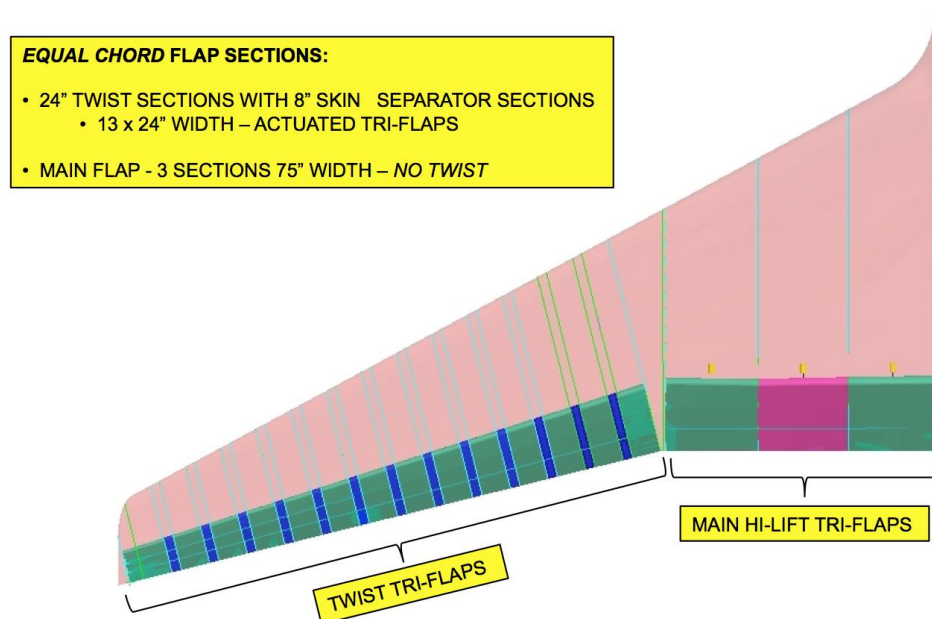
MAIN HI-LIFT TRI-FLAPS

TWIST TRI-FLAPS

Figure 3. GTM Wing Configured with the Variable Camber Continuous Trailing Edge Flap

Subsequently, Boeing Research & Technology conducted a joint study with NASA in 2012 to develop a system design of the VCCTEF[3,4] as shown in Fig. 3. This study was built upon the development of the original VCCTEF system for the NASA Generic Transport Model (GTM) which is essentially based on the Boeing 757 airframe. The VCCTEF design includes 14 spanwise sections attached to the outer wing and 3 spanwise sections attached to the inner wing, as shown in Fig. 3.[4] Each 24-inch section has three chordwise cambered flap segments that can be individually commanded. These cambered flaps are joined to the next section by a flexible and supported material (shown in blue) installed with the same shape as the camber and thus providing continuous flaps throughout the wing span with no drag producing gaps. The VCCTEF design results in the ability to control the wing twist shape along the wing span, thereby effectively producing a change to the wing twist to establish the best lift-to-drag ratio (L/D) at any aircraft gross weight or mission segment. The design wing twist on a traditional commercial transport is dictated by the aeroelastic deflection of a fixed "jig twist" shape applied during manufacturing. The design of this jig twist

is set for only one cruise configuration, usually for a 50% fuel loading or mid-point on the gross weight schedule. The VCCTEF offers different wing twist settings, hence different spanwise loadings, for each gross weight condition and also different settings for climb, cruise and descent. This ability is a major factor in obtaining best L/D flight conditions.

The flexibility of modern transport wings can cause a reduction in a flutter margin which can compromise aircraft stability. In addition, a flexible wing is more responsive to gust or maneuver loads which can lead to structural issues as well as compromised ride and handling qualities. In a previous study, a flutter analysis was conducted to examine the effect of increased flexibility of the GTM wing.[5] The baseline wing stiffness of the GTM is reduced by 50%. Table 1 shows the flutter speed prediction at 35,000 ft for the stiff wing GTM with the baseline stiffness and the flexible wing GTM with the reduced stiffness. The critical flutter mode for the flexible GTM wing is the first anti-symmetric bending mode which flutters at Mach 0.938 at an altitude of 35,000 ft.

	Symmetric Mode	Anti-Symmetric Mode
Stiff Wing GTM Flutter Mach @ 35K ft	1.358	1.310
Stiff Wing GTM Flutter Frequency @ 35K ft, Hz	4.31	3.87
Flexible Wing GTM Flutter Mach @ 35K ft	0.938	0.925
Flexible Wing GTM Flutter Frequency @ 35K ft, Hz	6.94	2.85

Table 1. Flutter Speed Prediction

The FAA (Federal Aviation Administration) requires aircraft certification to demonstrate a flutter margin of at least 15% above the dive speed which is normally determined from flight testing. For a maximum operating Mach 0.8, the dive speed may be estimated to be about 20% over the maximum operating Mach, or 0.96. Thus, the flutter clearance for this notional aircraft would require a minimum flutter speed of Mach 1.10 at 35,000 ft. The stiff wing GTM meets this flutter clearance but the flexible wing GTM does not. To increase the flutter speed, active flutter suppression is an option. Currently, active flutter suppression has not been certified for transport aircraft, but this situation may change as the FAA has begun to investigate certification requirements for active flutter suppression control for commercial transport aircraft.

To address the adaptive aeroelastic wing shaping control objective, a multidisciplinary design analysis optimization (MDAO) framework must be considered by incorporating the aerodynamic performance prediction together with aeroelasticity, flutter suppression control, and maneuver load alleviation control. The objective of the MDAO is to identify a desired wing flexibility that would provide the best overall aerodynamic, structural, aeroelasticity, and control benefits. For example, the wing stiffness could be optimized to maximize the aerodynamic performance at off-design cruise conditions with the least amount of control effort to maintain a flutter margin and maneuver load constraints. The MDAO would include the control synthesis directly in the MDAO process.

Flight control design of conventional aircraft has a long heritage with the single-axis flight control philosophy for pitch control by the elevator, roll control by the aileron, and yaw control by the rudder. The VCCTEF represents a new class of multi-functional flight control for future PAAW technology. This potentially could open up a new flight control paradigm. In the presence of multi-functional flight control surfaces such as the VCCTEF, a conventional flight control task such as a pitch command could be designed in conjunction with other flight control requirements particularly for flexible wing aircraft. These additional requirements may include: 1) drag minimization, 2) aeroelastic mode suppression, 3) maneuver load alleviation, and 4) gust load alleviation. In addressing these requirements, a flight control system could provide improvements in pilot handling qualities and passenger ride comfort.

To address all of these flight control objectives simultaneously can be a challenge in a flight control design. A multi-objective optimization framework can be developed to address the needs for satisfying multiple, competing flight control requirements. This paper will present a multi-objective flight control approach to address some of these multi-disciplinary interactions in a flexible wing aircraft employing PAAW technology. A multi-objective flight control system has been previously developed to simultaneously gain aerodynamic efficiency and maintain traditional pilot command-tracking tasks for guidance and navigation.[6,7] This study extends the previously developed multi-objective optimal control design to include gust and maneuver load alleviation objective in conjunction with the aeroelastic mode suppression and drag minimization objectives.

II. Adaptive Aeroelastic Wing Shaping Control Analysis

A. Drag Minimization Control

Aeroelastic deflections can affect aircraft aerodynamics. As an aircraft cruises, fuel is burned and the wing loading is reduced, thereby causing the lift distribution, hence the wing shape, to change. The change in the wing shape can cause a drag penalty since the wing shape no longer retains its optimal design shape. This particularly can be an important issue for light-weight airframes. Thus, aircraft with flexible wing structures can potentially become less fuel-efficient if there is no mechanism to compensate for aeroelastic deflections.

The elastic angle of attack contributes to the aircraft lift and drag. Aircraft wings are usually designed for optimal aerodynamics at a single point in the flight envelope. A typical design point for a transport aircraft wing is usually at the mid-point of a typical cruise profile where the fuel is half spent. As the fuel is burned off, the wing shape changes. The resulting static aeroelastic deflection alters the elastic angle of attack which in turn causes the lift distribution to be non-optimal. The net effect is a drag penalty at off-design flight conditions. In modern transport aircraft with flexible high-aspect ratio wings, special control devices are used to re-optimize the wing twist to compensate for the aeroelastic effect on aerodynamics.

The static aeroelastic equations for bending and torsion are given by

$$\rho A \frac{\partial^2 W}{\partial t^2} + \frac{\partial^2}{\partial x^2}\left(EI_{yy}\frac{\partial^2 W}{\partial x^2}\right) = \bar{l}\cos\Lambda - \rho A g \cos\Lambda + \frac{\partial \bar{m}}{\partial x}\cos\Lambda\sin\Lambda \tag{1}$$

$$\rho I_{xx}\frac{\partial^2\Theta}{\partial t^2} - \frac{\partial}{\partial x}\left(GJ\frac{\partial\Theta}{\partial x}\right) = \bar{m}\cos^2\Lambda - \rho A g e_{cg}\cos^2\Lambda \tag{2}$$

where $W(x,t)$ is the bending deflection, $\Theta(x,t)$ is the torsional twist, x is the coordinate of the elastic axis inclined from the aircraft pitch axis $\bar{y}$ by the sweep angle Λ as shown in Fig. 4, $\bar{l}(x,t)$ is the unsteady lift force, $\bar{m}(x,t)$ is the pitching moment in the streamwise direction along the elastic axis, $\rho A g$ is the wing weight distribution, e_{cg} is the offset of the center of mass from the elastic axis (positive when the center of mass lies forward of the elastic center), and the mass and elastic properties ρA, ρI_{xx}, EI_{yy} and GJ are all defined with respect to the elastic axis.
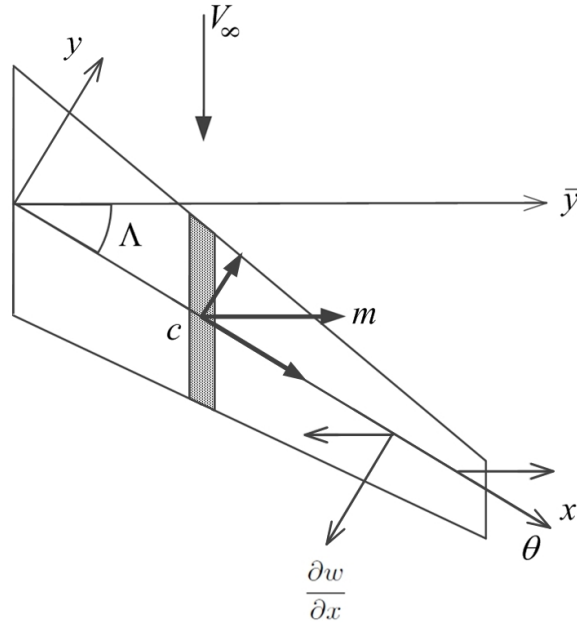

Figure 4. Swept Wing Coordinates

American Institute of Aeronautics and Astronautics

Using the aerodynamic strip theory, the unsteady sectional lift coefficient $c_L(x,t)$ is given by

$$c_L = \frac{\bar{l}}{q_\infty c} = c_{L_\alpha}(\alpha + \xi - \alpha_0) + C(k)c_{L_\delta}\delta + C(k)c_{L_\alpha}\left(\Theta\cos\Lambda - \frac{\partial W}{\partial x}\sin\Lambda + \frac{e_c\cos\Lambda}{V_\infty}\frac{\partial\Theta}{\partial t} - \frac{1}{V_\infty}\frac{\partial W}{\partial t}\right)$$
$$+ \frac{\pi c}{2V_\infty}\left(\cos\Lambda\frac{\partial\Theta}{\partial t} + \frac{e_m\cos\Lambda}{V_\infty}\frac{\partial^2\Theta}{\partial t^2} - \frac{1}{V_\infty}\frac{\partial^2 W}{\partial t^2}\right) \quad (3)$$

where q_∞ is the dynamic pressure, $c_{L_\alpha}(x)$ is the lift curve slope, $\alpha(t)$ is the angle of attack, $\xi(x)$ is the jig shape twist, $\alpha_0(x)$ is the zero-lift angle of attack, $c(x)$ is the wing chord in the streamwise direction, $c_{L_\delta}(x) = \begin{bmatrix} c_{L_{\delta_1}}(x) & c_{L_{\delta_2}}(x) \end{bmatrix}$

$\cdots \quad c_{L_{\delta_n}}(x) \end{bmatrix}^\top$ is a vector of the lift control derivatives, $\delta(t) = \begin{bmatrix} \delta_1(t) & \delta_2(t) & \cdots & \delta_n(t) \end{bmatrix}^\top$ is a vector of the flap deflections, $e_c(x)$ is the offset of the elastic center from the three-quarter-chord point (positive when the elastic center lies forward of the three-quarter-chord point), ρ_∞ is the air density, and $C(k)$ is Theodorsen's function of the reduced frequency parameter $k = \frac{\omega c}{2V_\infty}$ for the elastic wing.

The streamwise unsteady sectional pitching moment coefficient $c_m(x,t)$ is given by

$$c_m = \frac{\bar{m}}{q_\infty c^2} = c_{m_{ac}} + C(k)c_{m_\delta}\delta + \frac{e}{c}\left[c_{L_\alpha}(\alpha + \xi - \alpha_0) + C(k)c_{L_\delta}\delta\right]$$
$$+ C(k)\frac{e}{c}c_{L_\alpha}\left(\Theta\cos\Lambda - \frac{\partial W}{\partial x}\sin\Lambda + \frac{e_c\cos\Lambda}{V_\infty}\frac{\partial\Theta}{\partial t} - \frac{1}{V_\infty}\frac{\partial W}{\partial t}\right) - \frac{\pi e_m}{2V_\infty}\left(\frac{e_m\cos\Lambda}{V_\infty}\frac{\partial^2\Theta}{\partial t^2} - \frac{1}{V_\infty}\frac{\partial^2 W}{\partial t^2}\right)$$
$$- \frac{\pi e_c\cos\Lambda}{2V_\infty}\frac{\partial\Theta}{\partial t} - \frac{\pi c^2\cos\Lambda}{64V_\infty^2}\frac{\partial^2\Theta}{\partial t^2} \quad (4)$$

where $c_{m_{ac}}(x)$ is the pitching moment coefficient about the aerodynamic center, $c_{m_\delta}(x) = \begin{bmatrix} c_{m_{\delta_1}}(x) & c_{m_{\delta_2}}(x) & \cdots \end{bmatrix}$

$c_{m_{\delta_n}}(x) \end{bmatrix}^\top$ is a vector of the pitching moment control derivatives, $e(x)$ is the offset of the aerodynamic center from the elastic center (positive when the aerodynamic center lies forward of the elastic center), and $e_m(x)$ is the offset of the elastic center from the mid-chord point (positive when the elastic center lies forward of the mid-chord point).

The cruise condition dictates that the total lift L on the aircraft is equal to the weight W of the aircraft. So,

$$L = W \quad (5)$$

The wing lift typically constitutes at least 90% of the total lift of a typical transport aircraft. For a given design gross weight, air speed, and altitude, a design aircraft lift coefficient is computed as

$$C_L^* = \sqrt{\frac{W}{q_\infty S}} \quad (6)$$

where S is the wing reference area.

For steady state aerodynamics, the generalized rigid aerodynamic force vector is computed as

$$Q_r = \begin{bmatrix} \int_0^L \Phi^\top(x)l_r dx \\ \int_0^L \Psi^\top(x)m_r dx \end{bmatrix} = Q_0 + Q_\alpha\alpha + Q_\delta\delta \quad (7)$$

where $\Theta(x) = \begin{bmatrix} \Theta_1(x) & \Theta_2(x) & \cdots & \Theta_N(x) \end{bmatrix}^\top$ and $\Psi(x) = \begin{bmatrix} \Psi_1(x) & \Psi_2(x) & \cdots & \Psi_N(x) \end{bmatrix}^\top$ are vectors of the bending mode shape functions and torsional mode shape functions, respectively, and

$$l_r = \left[c_{L_\alpha}(\alpha + \xi - \alpha_0) + c_{L_\delta}\delta\right]q_\infty c\cos\Lambda - \rho Ag\cos\Lambda$$
$$+ \frac{\partial}{\partial x}\left\{c_{m_{ac}} + c_{m_\delta}\delta + \frac{e}{c}\left[c_{L_\alpha}(\alpha + \xi - \alpha_0) + c_{L_\delta}\delta\right]\right\}q_\infty c^2\cos\Lambda\sin\Lambda \quad (8)$$

$$m_r = \left\{c_{m_{ac}} + c_{m_\delta}\delta + \frac{e}{c}\left[c_{L_\alpha}(\alpha + \xi - \alpha_0) + c_{L_\delta}\delta\right]\right\}q_\infty c^2\cos^2\Lambda - \rho Age_{cg}\cos^2\Lambda \quad (9)$$

American Institute of Aeronautics and Astronautics

The generalized displacement is then expressed as

$$q = \left(K + q_\infty \frac{K_a}{q_\infty} \right)^{-1} (Q_0 + Q_\alpha \alpha + Q_\delta \delta) \tag{10}$$

where K is the structural stiffness matrix, K_a is the aerodynamic stiffness matrix, and $q = \begin{bmatrix} w_1 & w_2 & \cdots & w_N & \theta_1 \\ \theta_2 & \cdots & \theta_N \end{bmatrix}^\top$ is a vector of the generalized coordinates which form the displacement solutions

$$W(x) = \sum_{i=1}^{N} \Phi_i(x) w_i \tag{11}$$

$$\Theta(x) = \sum_{i=1}^{N} \Psi_i(x) \theta_i \tag{12}$$

Since the generalized rigid aerodynamic force is a function of the angle of attack α and flap deflection vector δ, the wing bending and torsional deflections are also functions of α and δ. This is written by

$$W(x) = W_0(x) + W_\alpha(x) \alpha + W_\delta(x) \delta \tag{13}$$

$$\Theta(x) = \Theta_0(x) + \Theta_\alpha(x) \alpha + \Theta_\delta(x) \delta \tag{14}$$

The local aeroelastic angle of attack on a swept wing is influenced by the bending and torsional deflections according to

$$\alpha_c = \alpha + \xi - \alpha_0 + \frac{c_{L_\delta}}{c_{L_\alpha}} \delta + [\Theta_0(x) + \Theta_\alpha(x) \alpha + \Theta_\delta(x) \delta] \cos\Lambda - \frac{\partial}{\partial x} [W_0(x) + W(x) \alpha + W_\delta(x) \delta] \sin\Lambda \tag{15}$$

At the design condition, the optimal lift distribution can be achieved by properly selecting the jig twist $\xi(x)$. This optimal lift distribution is expressed as

$$\Gamma = \frac{1}{2} V_\infty c c_L \tag{16}$$

The aerodynamic drag coefficient at the design condition is expressed in a parabolic drag polar as

$$C_D^* = C_{D_0}^* + \frac{C_L^{*2}}{\pi A R \varepsilon^*} \tag{17}$$

where $C_{D_0}^*$ is parasitic drag which includes the skin friction drag and transonic wave drag, AR is the wing aspect ratio, and $0 < \varepsilon^* < 1$ is the span efficiency factor.

The jig twist refers to the geometric twist that is built into the wing construction process during manufacturing. A jig-shape wing is generally of a planar planform. As the wing deflects under loading at the design cruise condition, the jig twist would compensate for the local aeroelastic angle of attack to achieve the optimal lift distribution. When the aircraft operates at off-design flight conditions, the design lift distribution can no longer be maintained. Consequently, a loss in the span efficiency factor results and causes an increase in the induced drag. At an off-design lift coefficient $C_L > C_L^*$, an incremental lift coefficient ΔC_L is required to trim the aircraft at an incremental angle of attack $\Delta\alpha$, then the change the lift distribution without aeroelastic compensation by wing shaping control is given by

$$\Delta\Gamma = \frac{1}{2} V_\infty c c_{L_\alpha} \Delta\alpha \left[\Theta_\alpha(x) \cos\Lambda - \frac{\partial W_\alpha(x)}{\partial x} \sin\Lambda \right] \tag{18}$$

The change in the lift distribution results in a reduction in the span efficiency factor which affects the induced drag. The aerodynamic drag can be expressed as

$$C_D = C_{D_0}^* + \Delta C_{D_0} + \frac{(C_L^* + \Delta C_L)^2}{\pi A R \varepsilon} \tag{19}$$

where $\varepsilon < \varepsilon^*$ for non-optimal lift distribution.

The parasitic drag usually is a convex function of the angle of attack. So, if the parasitic drag $C_{D_0}^*$ at the design condition is a minimum, then $\Delta C_{D_0} > 0$.

With aeroelastic compensation, the lift distribution can be optimized with a positive flap deflection δ to achieve the same incremental lift coefficient ΔC_L with a reduced incremental angle of attack $\Delta\alpha^*$. This optimized lift distribution is expressed as

$$\Delta\Gamma^* = \frac{1}{2}V_\infty cc_{L_\alpha}\Delta\alpha^* \left[\Theta_\alpha(x)\cos\Lambda - \frac{\partial W_\alpha(x)}{\partial x}\sin\Lambda\right] + \frac{1}{2}V_\infty cc_{L_\delta}\delta + \frac{1}{2}V_\infty cc_{L_\delta}\delta \left[\Theta_\delta(x)\cos\Lambda - \frac{\partial W_\delta(x)}{\partial x}\sin\Lambda\right] \quad (20)$$

Assuming the optimal span efficiency factor ε^* is achieved, then the aerodynamic drag due to aeroelastic wing shaping control is expressed as

$$C_D = C_{D_0}^* + \Delta C_{D_0}^* + \frac{(C_L^* + \Delta C_L)^2}{\pi AR\varepsilon^*} \quad (21)$$

A drag reduction is then obtained as

$$\Delta C_D = \Delta C_{D_0} - \Delta C_{D_0}^* + \left(\frac{1}{\varepsilon} - \frac{1}{\varepsilon^*}\right)\frac{(C_L^* + \Delta C_L)^2}{\pi AR} \quad (22)$$

It can be seen that the drag reduction comes from both the induced drag and the parasitic drag since $\Delta C_{D_0}^* < \Delta C_{D_0}$ because $\Delta\alpha^* < \Delta\alpha$. Thus, aeroelastic wing shaping control can offer a potential drag reduction benefit for fuel savings in transport aircraft.

In general, the drag minimization control can be solved by a coupled aerodynamic-structural optimization. This optimization can be performed off-line to establish a schedule of flap settings based on the aircraft gross weight and flight conditions. Aerodynamic-structural optimization studies as well as a wind tunnel experiment have been conducted to assess the drag reduction benefit of the VCCTEF.[8–10] These studies show a drag reduction benefit ranging from 1% to 6%. Figure 5 shows a typical solution of the aerodynamic-structural optimization of the spanwise lift distribution of the flexible wing GTM with the VCCTEF at an off-design cruise condition.[8]
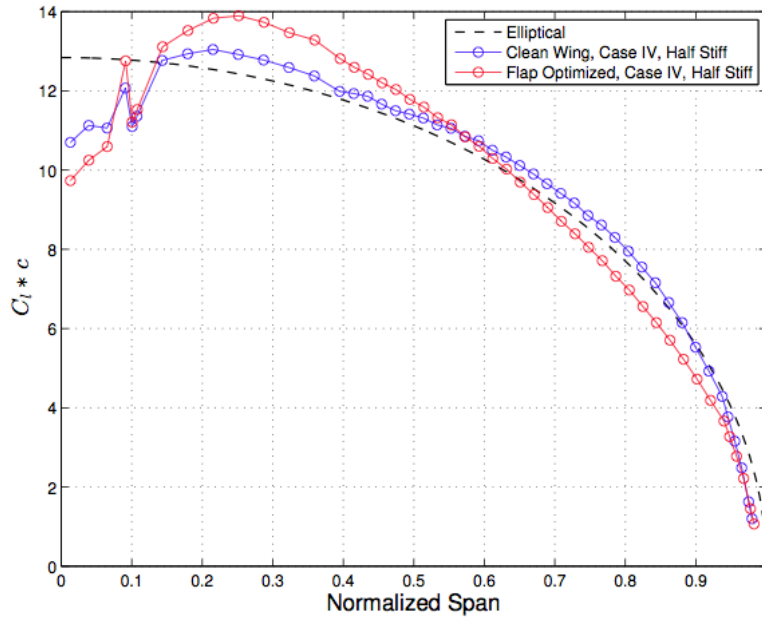

Figure 5. Optimized Spanwise Lift Distribution of Flexible Wing GTM at 30% Over Design C_L

In practice, variances in the aircraft gross weight and flight conditions can result in different performance characteristics than the optimal solutions obtained from the off-line aerodynamic-structural optimization. Thus, one approach in multi-objective flight control is to incorporate a real-time drag minimization control to compensate for operating variances. This real-time minimization control strategy has been developed recently and will be validated in a wind tunnel experiment.[11] The real-time drag minimization would require real-time drag and aeroelastic deflection measurements for estimating the aerodynamic characteristics of the flexible wing. This information is then used for the on-line optimization.

B. Load Alleviation Control

As aircraft wings become more flexible, maneuver and gust loads can result in potentially large load excursions. Dynamic responses due to a rapid flight maneuver such as a sudden pull-up or sharp roll can cause wing bending moments to increase rapidly. As a result, for high aspect ratio flexible wing aircraft, flight maneuvers must be executed in a manner so as to maintain flight loads to within the allowable limits. Multi-functional distributed flight control surfaces such as the VCCTEF can be deployed in these situations to achieve the required maneuver while reducing the maneuver loads. The maneuver load alleviation thus could be incorporated in the design of a flexible wing to reduce the wing structural weight.

As an example, consider the Truss-Braced Wing (TBW) aircraft equipped with a VCCTEF system as shown in Fig. 6. There are 10 flap sections, each with two chordwise cambered segments.[12]
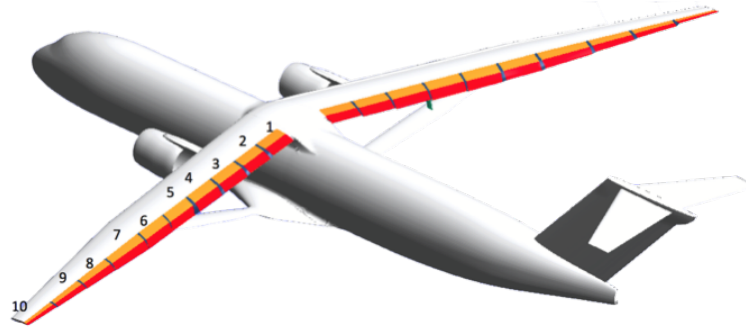

Figure 6. Truss-Braced Wing Aircraft with VCCTEF

A 2.5-g pull-up maneuver is commanded. Figure 7 shows the flapwise wing bending moment which is a maximum at the truss juncture.[12] The truss is designed to reduce the wing root bending moment as can be seen from the plot and effectively transfers the bending moment to the truss juncture. Without the VCCTEF deployment, the maximum bending moment occurs at the truss juncture. The VCCTEF is then deployed to alleviate the wing bending moment at the truss juncture. The optimal load alleviation occurs when both the wing root bending moment and bending moment at the truss juncture are equal. By optimization of the VCCTEF, the wing bending moment is reduced by 37%.[12]
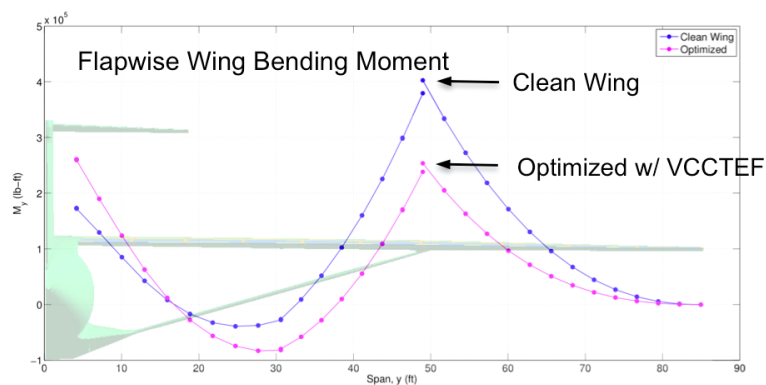

Figure 7. Wing Bending Moment for 2.5-g Pull-Up Maneuver

Figure 8 shows the lift distribution acting on the wing with and without the VCCTEF deployment.[12] To reduce the wing bending moment, the VCCTEF increases the wing lift inboard and decreases the wing lift outboard of the truss juncture. The VCCTEF effectively re-optimizes the spanwise lift distribution from a nearly elliptical lift distribution

American Institute of Aeronautics and Astronautics

for optimal aerodynamic performance at cruise to a lift distribution corresponding to a minimum wing bending moment. Thus, it can be seen that drag minimization control and maneuver load alleviation control produce an opposing effect. Therefore, maneuver load alleviation control cannot be achieved simultaneously with drag minimization control. In multi-objective control, this opposing effect is created by conflicting objectives. There exist multiple candidate optimal control solutions that lie on a Pareto optimal surface that provides a set of compromised solutions of a multi-objective optimization problem. The multi-objective optimal control thus provides a trade-off action to minimize one objective while not significantly degrading the other objective.
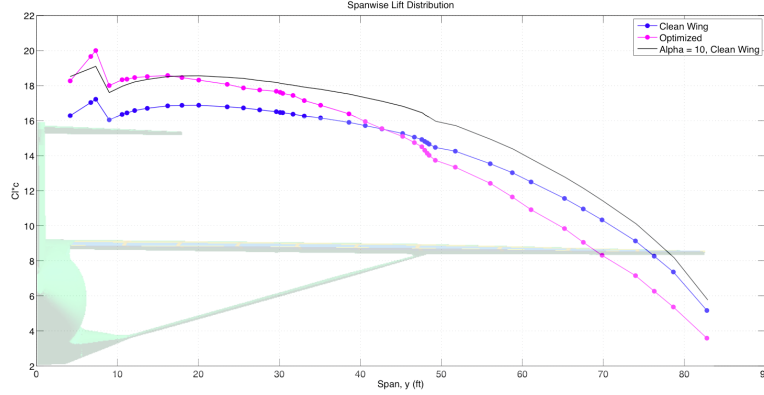

Figure 8. Wing Lift Distribution for Load Alleviation Control using VCCTEF

For the unsteady lift and pitching moment expressions in the previous section, we can express them in general as

$$l = l_0 + l_\alpha + l_\Theta \Theta + l_{\Theta_t} \frac{\partial \Theta}{\partial t} + l_{\Theta_{tt}} \frac{\partial^2 \Theta}{\partial t^2} + l_{W_x} \frac{\partial W}{\partial x} + l_{W_t} \frac{\partial W}{\partial t} + l_{W_{tt}} \frac{\partial^2 W}{\partial t^2} + l_\delta \delta + l_{\dot\delta} \dot\delta + l_{\ddot\delta} \ddot\delta \quad (23)$$

$$m = m_0 + m_\alpha \alpha + m_\Theta \Theta + m_{\Theta_t} \frac{\partial \Theta}{\partial t} + m_{\Theta_{tt}} \frac{\partial^2 \Theta}{\partial t^2} + m_{W_x} \frac{\partial W}{\partial x} + m_{W_t} \frac{\partial W}{\partial t} + m_{W_{tt}} \frac{\partial^2 W}{\partial t^2} + m_\delta \delta + m_{\dot\delta} \dot\delta + m_{\ddot\delta} \ddot\delta \quad (24)$$

where $l(x,t)$ and $m(x,t)$ are the expressions in the right hand sides of Eqs. (1) and (2).

The weak form expression of the aeroelastic equations using a finite-element method or other equivalent discretization is given by

$$M\ddot{q} + Kq = Q_0 + Q_\alpha \alpha + Q_q q + Q_{\dot q} \dot q + Q_{\ddot q} \ddot q + Q_\delta \delta + Q_{\dot\delta} \dot\delta + Q_{\ddot\delta} \ddot\delta \quad (25)$$

where M is the structural mass matrix, K is the complex stiffness matrix which accounts for structural damping, Q is the generalized force, and the subscripts denote the partial derivatives of the generalized force with respect to the subscript variables.

The wing flapwise bending moment and torsional pitching moment are computed as

$$M_x = GJ \frac{\partial \Theta}{\partial x} = GJ \sum_{i=1}^{N} \Psi_i'(x) \theta_i$$
$$= GJ\Psi'(x) \begin{bmatrix} 0 & I \end{bmatrix} K^{-1} \left(-M\ddot{q} + Q_0 + Q_\alpha \alpha + Q_q q + Q_{\dot q} \dot q + Q_{\ddot q} \ddot q + Q_\delta \delta + Q_{\dot\delta} \dot\delta + Q_{\ddot\delta} \ddot\delta \right) \quad (26)$$

$$M_y = EI_{yy} \frac{\partial^2 W}{\partial x^2} = EI_{yy} \sum_{i=1}^{N} \Phi_i''(x) w_i$$
$$= EI\Phi''(x) \begin{bmatrix} I & 0 \end{bmatrix} K^{-1} \left(-M\ddot{q} + Q_r + Q_q q + Q_{\dot q} \dot q + Q_{\ddot q} \ddot q + Q_\delta \delta + Q_{\dot\delta} \dot\delta + Q_{\ddot\delta} \ddot\delta \right) \quad (27)$$

The bending moment at a critical location on the wing can be evaluated from the expression above and expressed in general as

$$M_c = M_0 + M_\alpha \alpha + M_q q + M_{\dot q} \dot q + M_{\ddot q} \ddot q + M_\delta \delta + M_{\dot q} \dot\delta + M_{\ddot q} \ddot\delta \quad (28)$$

The maneuver load alleviation control can be formulated as a cost function with two control variables $\alpha(t)$ and $\delta(t)$

$$J(\alpha,\delta) = \frac{1}{2}\int_0^{t_f} M_c^2 \, dt \tag{29}$$

subject to Eq. (25), the lift constraint

$$C_L = \frac{nW}{q_\infty S} = C_{L_0} + C_{L_\alpha}\alpha + C_{L_q}q + C_{L_{\dot{q}}}\dot{q} + C_{L_{\ddot{q}}}\ddot{q} + C_{L_\delta}\delta + C_{L_{\dot{\delta}}}\dot{\delta} + C_{L_{\ddot{q}}}\ddot{q} < C_{L_{max}} \tag{30}$$

and local angle of attack constraint

$$\alpha_c < \alpha_{max} \tag{31}$$

where n is the load factor during a maneuver.

The lift constraint is to ensure the optimal control solution provides the correct lift for the flight maneuver not to exceed the maximum lift coefficient at which aerodynamic stall occurs. The maximum local angle of attack on a wing usually occurs at the wing root. Then by enforcing the local angle of attack constraint, the wing bending moment can be minimized by increasing lift at the wing root up to the maximum allowable value corresponding to α_{max} without causing the wing to stall.

The maneuver load alleviation control is then posed as an off-line optimization problem. A schedule of flap deflections and angle of attack can be obtained as functions of the load factor and the flight maneuver. This scheduling approach is useful for prescribed flight maneuvers with known aerodynamic characteristics. For real-time maneuver load alleviation control, the off-line optimization has to be converted into a real-time optimal control problem. This is to be presented in the following sections.

III.   Aeroservoelastic Model Formulation

To design a multi-objective flight control for drag minimization and load alleviation, an aeroservoelastic (ASE) model of a flexible wing aircraft equipped with the VCCTEF is developed. The ASE model includes the rigid aircraft flight dynamics, wing dynamic aeroelasticity, flight control actuator dynamics of the flap system, and servo-motor dynamics.[13,14]

In general, the rigid aircraft flight dynamic equation is expressed as

$$M_r\dot{x}_r = Q_r\dot{x}_r + P_r x_r + D_r\delta_r + V_{rn}\ddot{q} + (T_{rn} + 0.5T_{rc})\dot{q} + \left[S_{rn} + 0.5S_{rc} + a_4\left(\frac{2V_\infty}{c}\right)T_{rc}\right]q + S_{rc}y + \left(\frac{2V_\infty}{c}\right)T_{rc}z$$

$$+ F_{rn}\ddot{\delta} + (E_{rn} + 0.5E_{rc})\dot{\delta} + \left[D_{rn} + 0.5D_{rc} + a_4\left(\frac{2V_\infty}{c}\right)E_{rc}\right]\delta + D_{rc}v + \left(\frac{2V_\infty}{c}\right)E_{rc}w \tag{32}$$

where $x_r(t)$ is the rigid aircraft state vector, $q(t)$ is the generalized displacement vector of the wing, $y(t)$ and $z(t)$ are the aerodynamic lag state vectors for the wing structural dynamics, $\delta_r(t)$ is the rigid aircraft flight control surface deflection vector, $\delta(t)$ is the VCCTEF deflection vector, $v(t)$ and $w(t)$ are the aerodynamic lag state vectors for the VCCTEF actuator dynamics, the upper case variables are matrices, the subscript r denotes a rigid aircraft quantity, and the subscripts n and c denote non-circulatory and circulatory quantities according to the Theodorsen's theory.

The rigid aircraft state vector $x_r(t)$ in the pitch axis normally includes the altitude $h(t)$, airspeed $V(t)$, angle of attack $\alpha(t)$, pitch rate $q(t)$ (not to be confused with the generalized displacement vector), and pitch angle $\theta(t)$. In the roll and yaw axes, the rigid aircraft state vector includes the angle of sideslip $\beta(t)$, roll rate $p(t)$, yaw rate $r(t)$, bank angle $\phi(t)$, and heading angle $\psi(t)$. The rigid aircraft flight control surface deflection vector $\delta_r(t)$ includes the elevator deflection $\delta_e(t)$ for the pitch axis, the aileron deflection $\delta_a(t)$ for the roll axis, and the rudder deflection $\delta_r(t)$ for the yaw axis.

The aerodynamic lag states account for the unsteady aerodynamic effect which is represented by the reduced frequency-dependent Theodorsen's function. The R. T. Jones approximation is used to convert the Theodorsen's function into a time-domain representation by the aerodynamic lag states.

Using the finite-element formulation, the aeroelastic equation of the wing structure is discretized as

$$(M_s + M_{an})\ddot{q} + (C_s + C_{an} + 0.5C_{ac})\dot{q} + \left[K_s + 0.5K_{ac} + a_4\left(\frac{2V_\infty}{c}\right)C_{ac}\right]q + K_{ac}y + \left(\frac{2V_\infty}{c}\right)C_{ac}z = Q_e\dot{x}_r + P_e x_r$$

$$+ F_{en}\ddot{\delta} + (E_{en} + 0.5E_{ec})\dot{\delta} + \left[D_{en} + 0.5D_{ec} + a_4\left(\frac{2V_\infty}{c}\right)E_{ec}\right]\delta + D_{ec}v + \left(\frac{2V_\infty}{c}\right)E_{ec}w \tag{33}$$

where the subscript s denotes a structural dynamic quantity, the subscript a denotes an aerodynamic quantity due to the unsteady aerodynamic effect, and the subscript e denotes an aeroelastic quantity associated with the wing aeroelasticity.

The aerodynamic lag state equations for the wing structural dynamics obtained from the R. T. Jones approximation are

$$\ddot{y} + a_3 \left(\frac{2V_\infty}{c} \right) \dot{y} + a_2 \left(\frac{2V_\infty}{c} \right)^2 y = a_4 \left(\frac{2V_\infty}{c} \right) \dot{q} + 0.5a_2 \left(\frac{2V_\infty}{c} \right)^2 q \tag{34}$$

$$\ddot{z} + a_3 \left(\frac{2V_\infty}{c} \right) \dot{z} + a_2 \left(\frac{2V_\infty}{c} \right)^2 z = a_5 \left(\frac{2V_\infty}{c} \right) \dot{q} + a_6 \left(\frac{2V_\infty}{c} \right)^2 q \tag{35}$$

The actuator dynamic equation of the VCCTEF is expressed as

$$M_\delta \ddot{\delta} + C_\delta \dot{\delta} + K_\delta \delta = Q_\delta \dot{x}_r + P_\delta x_r + V_{\delta n} \ddot{q} + (T_{\delta n} + 0.5T_{\delta c}) \dot{q} + \left[S_{\delta n} + 0.5S_{\delta c} + a_4 \left(\frac{2V_\infty}{c} \right) T_{\delta c} \right] q$$
$$+ S_{\delta c} y + \left(\frac{2V_\infty}{c} \right) T_{\delta c} z + F_{\delta n} \ddot{\delta} + (E_{\delta n} + 0.5E_{\delta c}) \dot{\delta} + \left[D_{\delta n} + 0.5D_{\delta c} + a_4 \left(\frac{2V_\infty}{c} \right) E_{\delta c} \right] \delta + D_{\delta c} v$$
$$+ \left(\frac{2V_\infty}{c} \right) E_{\delta c} w + \tau_\delta \tag{36}$$

where $\tau_\delta(t)$ is the motor torque.

The aerodynamic lag state equations for the actuator dynamics are

$$\ddot{v} + a_3 \left(\frac{2V_\infty}{c} \right) \dot{v} + a_2 \left(\frac{2V_\infty}{c} \right)^2 v = a_4 \left(\frac{2V_\infty}{c} \right) \dot{\delta} + 0.5a_2 \left(\frac{2V_\infty}{c} \right)^2 \delta \tag{37}$$

$$\ddot{w} + a_3 \left(\frac{2V_\infty}{c} \right) \dot{w} + a_2 \left(\frac{2V_\infty}{c} \right)^2 w = a_5 \left(\frac{2V_\infty}{c} \right) \dot{\delta} + a_6 \left(\frac{2V_\infty}{c} \right)^2 \delta \tag{38}$$

The actuator dynamics of the rigid aircraft flight control are assumed to be a first-order model

$$\dot{\delta}_r = -\lambda \left(\delta_r - \delta_{rc} \right) \tag{39}$$

where $\lambda > 0$ is the actuator rate vector and $\delta_{rc}(t)$ is the command vector of the rigid aircraft flight control.

The servo-motor dynamics for the VCCTEF are formed by a PID feedback control law

$$\dot{e} = \delta - \delta_c \tag{40}$$

$$\tau_\delta = k_p \left(\delta - \delta_c \right) + k_i e + k_d \dot{\delta} \tag{41}$$

where $e(t)$ is the integral error of the VCCTEF deflection command $\delta_c(t)$.

The fully coupled ASE flight dynamic model is shown in Table 2.

American Institute of Aeronautics and Astronautics

$$
\begin{bmatrix}
M_r - Q_r & 0 & 0 & -V_{rn} & 0 & 0 & 0 & 0 & -F_{rn} & 0 & 0 & 0 \\
0 & I & 0 & 0 & 0 & 0 & 0 & 0 & 0 & 0 & 0 & 0 \\
0 & 0 & I & 0 & 0 & 0 & 0 & 0 & 0 & 0 & 0 & 0 \\
-Q_e & 0 & 0 & M_s + M_{an} & 0 & 0 & 0 & 0 & -F_{en} & 0 & 0 & 0 \\
0 & 0 & 0 & 0 & I & 0 & 0 & 0 & 0 & 0 & 0 & 0 \\
0 & 0 & 0 & 0 & 0 & I & 0 & 0 & 0 & 0 & 0 & 0 \\
0 & 0 & 0 & 0 & 0 & 0 & I & 0 & 0 & 0 & 0 & 0 \\
0 & 0 & 0 & 0 & 0 & 0 & 0 & I & 0 & 0 & 0 & 0 \\
0 & 0 & 0 & 0 & 0 & 0 & 0 & 0 & I & 0 & 0 & 0 \\
-Q_\delta & 0 & 0 & -V_{\delta n} & 0 & 0 & 0 & 0 & M_\delta - F_{\delta n} & 0 & 0 & 0 \\
0 & 0 & 0 & 0 & 0 & 0 & 0 & 0 & 0 & I & 0 & 0 \\
0 & 0 & 0 & 0 & 0 & 0 & 0 & 0 & 0 & 0 & I & 0 \\
0 & 0 & 0 & 0 & 0 & 0 & 0 & 0 & 0 & 0 & 0 & I \\
0 & 0 & 0 & 0 & 0 & 0 & 0 & 0 & 0 & 0 & 0 & 0 \\
0 & 0 & 0 & 0 & 0 & 0 & 0 & 0 & 0 & 0 & 0 & 0
\end{bmatrix}
\begin{Bmatrix}
\dot{x}_r \\ \dot{q} \\ \dot{y} \\ \dot{z} \\ \ddot{q} \\ \ddot{y} \\ \ddot{z} \\ \dot{\delta} \\ \dot{v} \\ \ddot{w} \\ \ddot{\delta} \\ \ddot{v} \\ \ddot{w} \\ \dot{\delta}_r \\ \dot{e}
\end{Bmatrix}
=
$$

$$
\begin{bmatrix}
S_{rm} + 0.5 S_{rc} + a_4\left(\frac{2V_\infty}{c}\right)T_{rc} & S_{rc} & \left(\frac{2V_\infty}{c}\right)T_{rc} & T_{rm} + 0.5 T_{rc} & 0 \\
0 & 0 & 0 & I & 0 \\
0 & 0 & 0 & 0 & I \\
-\left[K_s + 0.5 K_{ac} + a_4\left(\frac{2V_\infty}{c}\right)C_{ac}\right] & -K_{ac} & -\left(\frac{2V_\infty}{c}\right)C_{ac} & -\left(C_s + C_{an} + 0.5 C_{ac}\right) & 0 \\
0.5 a_2\left(\frac{2V_\infty}{c}\right)^2 & -a_2\left(\frac{2V_\infty}{c}\right)^2 & 0 & a_4\left(\frac{2V_\infty}{c}\right) & -a_3\left(\frac{2V_\infty}{c}\right) \\
a_6\left(\frac{2V_\infty}{c}\right)^2 & 0 & -a_2\left(\frac{2V_\infty}{c}\right)^2 & a_5\left(\frac{2V_\infty}{c}\right) & 0 \\
0 & 0 & 0 & 0 & 0 \\
0 & 0 & 0 & 0 & 0 \\
0 & 0 & 0 & 0 & 0 \\
S_{\delta n} + 0.5 S_{\delta c} + a_4\left(\frac{2V_\infty}{c}\right)T_{\delta c} & S_{\delta c} & \left(\frac{2V_\infty}{c}\right)T_{\delta c} & T_{\delta n} + 0.5 T_{\delta c} & 0 \\
0 & 0 & 0 & 0 & 0 \\
0 & 0 & 0 & 0 & 0 \\
0 & 0 & 0 & 0 & 0 \\
0 & 0 & 0 & 0 & 0 \\
0 & 0 & 0 & 0 & 0
\end{bmatrix}
\begin{Bmatrix}
P_r \\ 0 \\ 0 \\ P_e \\ 0 \\ 0 \\ 0 \\ 0 \\ 0 \\ P_\delta \\ 0 \\ 0 \\ 0 \\ 0
\end{Bmatrix}
$$

$$
\left[
\begin{array}{cccc|ccc|cc}
D_{rn}+0.5D_{rc}+a_4\left(\tfrac{2V_\infty}{c}\right)E_{rc} & D_{rc} & \left(\tfrac{2V_\infty}{c}\right)E_{rc} & E_{rn}+0.5E_{rc} & 0 & 0 & 0 & D_r & 0\\[2pt]
0 & 0 & 0 & 0 & 0 & 0 & 0 & 0 & 0\\
0 & 0 & 0 & 0 & 0 & 0 & 0 & 0 & 0\\
0 & 0 & 0 & 0 & 0 & 0 & 0 & 0 & 0\\[2pt]
D_{en}+0.5D_{ec}+a_4\left(\tfrac{2V_\infty}{c}\right)E_{ec} & D_{ec} & \left(\tfrac{2V_\infty}{c}\right)E_{ec} & E_{en}+0.5E_{ec} & 0 & 0 & 0 & 0 & 0\\[2pt]
0 & 0 & 0 & 0 & 0 & 0 & 0 & 0 & 0\\
0 & 0 & 0 & 0 & 0 & 0 & 0 & 0 & 0\\
\hline
-K_\delta+D_{\delta n}+0.5D_{\delta c}+a_4\left(\tfrac{2V_\infty}{c}\right)E_{\delta c}+k_p & D_{\delta c} & \left(\tfrac{2V_\infty}{c}\right)E_{\delta c} & -C_\delta+E_{\delta n}+0.5E_{\delta c}+k_d & I & 0 & 0 & 0 & 0\\[2pt]
0.5a_2\left(\tfrac{2V_\infty}{c}\right)^2 & -a_2\left(\tfrac{2V_\infty}{c}\right)^2 & 0 & a_4\left(\tfrac{2V_\infty}{c}\right) & 0 & I & 0 & 0 & 0\\[2pt]
a_6\left(\tfrac{2V_\infty}{c}\right) & 0 & -a_2\left(\tfrac{2V_\infty}{c}\right)^2 & a_5\left(\tfrac{2V_\infty}{c}\right) & -a_3\left(\tfrac{2V_\infty}{c}\right) & -a_3\left(\tfrac{2V_\infty}{c}\right) & 0 & 0 & 0\\[2pt]
0 & 0 & 0 & 0 & 0 & 0 & 0 & k_i & 0\\
0 & 0 & 0 & 0 & 0 & 0 & 0 & 0 & 0\\
0 & 0 & 0 & 0 & 0 & 0 & 0 & 0 & 0\\
\hline
0 & 0 & 0 & 0 & 0 & 0 & 0 & -\lambda & 0\\
I & 0 & 0 & 0 & 0 & 0 & 0 & 0 & 0
\end{array}
\right]
\begin{Bmatrix}
x_r \\ q \\ y \\ z \\ \dot{q} \\ \dot{y} \\ \dot{z} \\ \hline \delta \\ v \\ w \\ \dot{\delta} \\ \dot{v} \\ \dot{w} \\ \hline \delta_r \\ e
\end{Bmatrix}
+
\left[
\begin{array}{cc}
0 & 0\\
0 & 0\\
0 & 0\\
0 & 0\\
0 & 0\\
0 & 0\\
0 & 0\\
0 & 0\\
0 & 0\\
0 & 0\\
0 & -k_p\\
0 & 0\\
0 & 0\\
\lambda & 0\\
0 & -I
\end{array}
\right]
\begin{bmatrix} \delta_{rc} \\ \delta_c \end{bmatrix}
$$

Table 2. Coupled Aeroservoelastic Flight Dynamic Model

Let $x_q(t) = \begin{bmatrix} q(t) & y(t) & z(t) & \dot{q}(t) & \dot{y}(t) & \dot{z}(t) \end{bmatrix}^\top$, $x_\delta(t) = \begin{bmatrix} \delta(t) & v(t) & w(t) & \dot{\delta}(t) & \dot{v}(t) & \dot{w}(t) \end{bmatrix}^\top$, $x_s(t) = \begin{bmatrix} \delta_r(t) & e(t) \end{bmatrix}^\top$, and $u(t) = \begin{bmatrix} \delta_{rc}(t) & \delta_c(t) \end{bmatrix}^\top$. Then, the ASE state space model can be expressed as

$$\begin{bmatrix} M_{rr} & M_{rq} & M_{r\delta} & M_{rs} \\ M_{qr} & M_{qq} & M_{q\delta} & M_{qs} \\ M_{\delta r} & M_{\delta q} & M_{\delta\delta} & M_{\delta s} \\ M_{sr} & M_{sq} & M_{s\delta} & M_{ss} \end{bmatrix} \begin{bmatrix} \dot{x}_r \\ \dot{x}_q \\ \dot{x}_\delta \\ \dot{x}_s \end{bmatrix} = \begin{bmatrix} S_{rr} & S_{rq} & S_{r\delta} & S_{rs} \\ S_{qr} & S_{qq} & S_{q\delta} & S_{qs} \\ S_{\delta r} & S_{\delta q} & S_{\delta\delta} & S_{\delta s} \\ S_{sr} & S_{sq} & S_{s\delta} & S_{ss} \end{bmatrix} \begin{bmatrix} x_r \\ x_q \\ x_\delta \\ x_s \end{bmatrix} + \begin{bmatrix} T_r \\ T_e \\ T_\delta \\ T_s \end{bmatrix} u \tag{42}$$

This is more compactly written as

$$\dot{x} = Ax + Bu + w \tag{43}$$

where $x(t) = \begin{bmatrix} x_r(t) & x_q(t) & x_\delta(t) & x_s(t) \end{bmatrix}^\top$ and $w(t)$ is the gust disturbance (not to be confused with the aerodynamic lag state).

The output which is an acceleration measurement is computed as

$$\ddot{u} = \Phi\ddot{q} = \Phi E \dot{x}_q \tag{44}$$

where Φ is the matrix of eigenvectors and $E = \begin{bmatrix} 0 & 0 & 0 & I & 0 & 0 \end{bmatrix}$ such that $\ddot{q} = E\dot{x}_q$.

Then,

$$\ddot{u} = \Phi E G(Ax + Bu) \tag{45}$$

where $G = \begin{bmatrix} 0 & I & 0 & 0 \end{bmatrix}$ such that $\dot{x}_e = G\dot{x}$.

For a given acceleration location, then

$$\ddot{u}_c = F\ddot{u} = F\Phi E G(Ax + Bu) \tag{46}$$

where F is determined from the location of the acceleration measurement.

Let $y = \ddot{u}_c$ be the output, then

$$y = Cx + Du \tag{47}$$

where

$$C = F\Phi E G A \tag{48}$$

$$D = F\Phi E G B \tag{49}$$

The aircraft drag is expressed as

$$C_D = C_{D_0} + \left(C_{L_0} + C_{L_{\dot{x}}}\dot{x} + C_{L_x}x + C_{L_u}u \right)^\top K \left(C_{L_{\dot{x}}}\dot{x} + C_{L_x}x + C_{L_u}u \right) \tag{50}$$

Therefore the incremental drag is computed as

$$\Delta C_D = C_{D_x}x + C_{D_u}u + x^\top C_{D_{x^2}}x + x^\top C_{D_{xu}}u + u^\top C_{D_{u^2}}u \tag{51}$$

The wing bending moment is expressed in general as

$$M_y = M_x x + M_u u + M_w w \tag{52}$$

where $M_w w(t)$ is a bending moment component due to the gust disturbance.

IV.   Multi-Objective Flight Control for Drag Minimization and Load Alleviation

Multi-objective flight control design is an enabling feature of PAAW technology. A typical flight control design usually takes into account different sets of requirements for performance and stability that must be considered during a design process. Performance in the context of flight control usually implies the ability for a flight control system to follow a pilot command. However, in this study, a new notion of aerodynamic performance is introduced into the flight control framework. The goal of the new vehicle is to achieve low drag through adaptive aeroelastic wing shaping control actuation. Thus, drag penalty due to the VCCTEF should be considered in a flight control design. Hence, a new concept of multi-objective flight control has been proposed to not only achieve a pilot command-following objective but also a drag reduction objective[1,6,7] during maneuvers.

Stability is of paramount importance for any flight vehicle. Structural flexibility of airframes can cause significant aeroelastic interactions that can degrade vehicle stability margins, potentially leading to loss of control. There exists a trade-off between structural flexibility and flutter margins. With increased wing flexibility, a flutter margin could possibly occur below the FAA flutter clearance requirement. Thus, a flight control system must be able to stabilize any potential flutter modes. For obvious reasons, it is generally not acceptable to design an unstable transport aircraft that relies on feedback control for flutter suppression. Thus, in practice, an aeroelastically stable airframe will always be required, but the increase in structural flexibility may manifest itself as an increase in the airframe response to flight loads. Then, the role of a flight control system would be relegated to stability augmentation for aeroelastic mode suppression as opposed to a more demanding task of aeroelastic stabilization. This is generally considered to be more acceptable in the certification of flexible aircraft flight control since existing aircraft flight control systems already include many stability augmentation features such as the yaw and pitch dampers to provide desired damping characteristics to meet pilot handling quality requirements.

Gust and maneuver load alleviation control is also an important part of the overall flight control strategy for flexible aircraft. As structural flexibility increases, the vehicle aeroelastic response to a wind gust disturbance or during a maneuver can result in handling and ride quality issues. Gust load alleviation control can reduce the aeroelastic response by reactive feedback control or predictive feedforward control using early detection turbulence sensors. Similarly, maneuver loads can be kept to within a required load envelope by means of maneuver load alleviation control.

In terms of control actuation, the VCCTEF is designed with dual purposes. The two inner chordwise flap segments are driven by shaped memory alloy (SMA) actuators which are slow actuators suitable only for changing the VCCTEF settings for cruise drag optimization either by scheduling or real-time drag optimization.[4] This is considered as a guidance feature that could be used in an auto-pilot cruise control. For fast-acting flight control functions, the outermost chordwise flap segment is designed to be a fast acting control surface driven by electro-mechanical actuators (EMA).[4] This flap segment is spanned the entire wing and is assumed to have the required bandwidth and control power for roll control and aeroelastic mode suppression control.

The multi-objective flight control framework is envisioned to comprise of the following objectives all acting in a synergistic manner: 1) traditional pilot command-following flight control, 2) drag minimization, 3) aeroelastic mode suppression, and 4) gust and maneuver load alleviation. Each of these objectives can be a major control system design in its own right. Thus, a multi-objective flight control system can be a complex flight control design that takes into account multiple competing requirements to achieve optimal flight control solutions that have the best compromise for these requirements. Figure 9 illustrates an architecture of a multi-objective flight control system.[7] In addition, a real-time drag minimization control strategy is included in the guidance loop.[11] This feature utilizes system identification methods to estimate aerodynamic parameters for the on-line optimization. The aerodynamic parameters are also used in the multi-objective flight control for drag minimization and load alleviation control.

The ASE state space model can be written as

$$\dot{x}_r = A_{rr}x_r + A_{re}x_e + B_r u_r + w_r \tag{53}$$

$$\dot{x}_e = A_{er}x_r + A_{ee}x_e + B_e u_e + w_e \tag{54}$$

where $x_r(t)$ is rigid-body state vector which is available for feedback, $x_e(t)$ is the elastic state vector including the actuator state vector of the VCCTEF dynamics which is not measured, $u_r(t)$ is the rigid aircraft control input vector, $u_e(t)$ is the VCCTEF control input vector, $w_r(t)$ is the disturbance to the rigid aircraft state, and $w_e(t)$ is the disturbance to the elastic state.
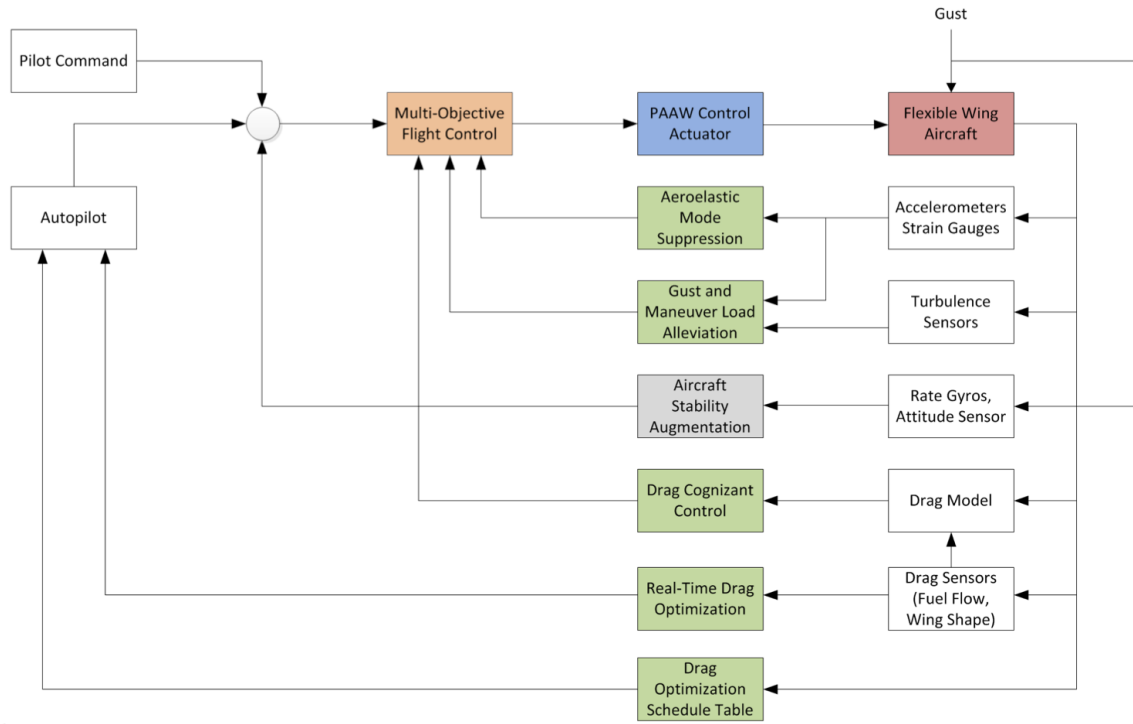
Figure 9. Multi-Objective Flight Control Architecture

The output vector which is measured by accelerometers or strain gauges is given by

$$y = Cx + Du = C_r x_r + C_e x_e + D_r u_r + D_e u_e \tag{55}$$

where $x(t) = \begin{bmatrix} x_r^\top(t) & x_e^\top(t) \end{bmatrix}^\top$ and $u(t) = \begin{bmatrix} u_r^\top(t) & u_e^\top(t) \end{bmatrix}^\top$.

We formulate a multi-objective infinite time-horizon cost function as follows:

$$J = J_r + J_e \tag{56}$$

where

$$J_r = \lim_{t_f \to \infty} \frac{1}{2} \int_0^{t_f} \left[(z-r)^\top Q_r (z-r) + u_r^\top R_r u_r \right] dt \tag{57}$$

$$J_e = \lim_{t_f \to \infty} \frac{1}{2} \int_0^{t_f} \left(x_e^\top Q_e x_e + u_e^\top R_e u_e + q_D \Delta C_D + M_y^\top q_M M_y \right) dt \tag{58}$$

The rigid aircraft controller $u_r(t)$ can be designed based on the cost function J_r to enable a rigid aircraft state $z(t) = F x_r(t)$ to track a command signal $r(t)$. The VCCTEF controller $u_e(t)$ is designed based on the total cost function J to provide drag minimization, aeroelastic mode suppression, and gust and maneuver load alleviation.

A. Rigid Aircraft Control with Disturbance Estimation

We proceed with the nominal rigid aircraft control design for the nominal rigid aircraft dynamics by formulating the Hamiltonian function

$$H = \frac{1}{2}(Fx_r - r)^\top Q_r (Fx_r - r) + \frac{1}{2} u_r^\top R_r u_r + \lambda^\top (A_{rr} x_r + B_r u_r) \tag{59}$$

where $\lambda(t)$ is the adjoint variable.

The adjoint equation and optimal control are obtained as

$$\dot{\lambda} = -\frac{\partial H^\top}{\partial x_r} = -F^\top Q_r (Fx_r - r) - A_{rr}^\top \lambda \tag{60}$$

$$\frac{\partial H^\top}{\partial u_r} = R_r u_r + B_r^\top \lambda = 0 \Rightarrow u_r = -R_r B_r^\top \lambda \tag{61}$$

subject to the transversality condition $\lambda(t_f) = 0$.

Let $\lambda(t) = P(t)x_r(t) + S(t)$. Then,

$$\dot{P}x_r + P\left(A_{rr}x_r - B_r R_r B_r^\top P x_r - B_r R_r B_r^\top S\right) + \dot{S} = -F^\top Q_r F x_r + F^\top Q_r r - A_{rr}^\top P x_r - A_{rr}^\top S \tag{62}$$

For the infinite time-horizon optimal control, $\dot{P} = 0$ and $\dot{S} = 0$. Therefore, we obtain

$$PA_{rr} + A_{rr}^\top P - PB_r R_r B_r^\top P + F^\top Q_r F = 0 \tag{63}$$

$$S = \left(A_{rr}^\top - PB_r R_r B_r^\top\right)^{-1} F^\top Q_r r \tag{64}$$

Then, the nominal rigid aircraft controller is given by

$$\bar{u}_r = K_{x_r} x_r + K_r r \tag{65}$$

where

$$K_{x_r} = -R_r B_r^\top P \tag{66}$$

$$K_r = -R_r B_r^\top \left(A_{rr}^\top - PB_r R_r B_r^\top\right)^{-1} F^\top Q_r \tag{67}$$

B. Disturbance Estimation

The closed-loop rigid aircraft dynamics then become

$$\dot{x}_r = (A_{rr} + B_r K_{x_r})x_r + B_r K_r r + A_{re} x_e + w_r \tag{68}$$

The predictor model of the rigid aircraft dynamics is formulated as

$$\dot{\hat{x}}_r = (A_{rr} + B_r K_{x_r})\hat{x}_r - B_r K_{x_r} x_r + A_{re}\hat{x}_e + B_r u_r + \hat{w}_r \tag{69}$$

where $\hat{w}_r(t)$ is the disturbance estimation of $w_r(t)$, $\dot{\hat{x}}_r(t)$ is the estimate of $\dot{x}_r(t)$ only for the purpose of the disturbance estimation and $\hat{x}_e(t)$ is the observer elastic state computed by the Kalman filter state estimation as

$$\dot{\hat{x}}_e = A_{ee}\hat{x}_e + A_{er}x_r + L(y - \hat{y}) + B_e u_e + \hat{w}_e \tag{70}$$

where $\hat{w}_e(t)$ is the disturbance estimation of $w_e(t)$

The plant modeling error of the rigid aircraft dynamics is formulated as

$$\varepsilon_r = \dot{\hat{x}}_r - \dot{x}_r = (A_{rr} + B_r K_{x_r})(\hat{x}_r - x_r) + A_{re}(\hat{x}_e - x_e) + \hat{w}_r - w_r \tag{71}$$

The estimate of the wing root bending moment is formulated as

$$\hat{M}_y = M_x \hat{x} + M_u u + M_{w_r} \hat{w}_r + M_{w_e} \hat{w}_e \tag{72}$$

Then, the wing root bending moment error is computed as

$$\varepsilon_M = \hat{M}_y - M_y = M_x \hat{x} + M_u u + M_{w_r} \hat{w}_r + M_{w_e} \hat{w}_e - M_y \tag{73}$$

where $M_y(t)$ is assumed to be available from a strain gauge measurement.

Then, minimizing the composite cost function

$$J = \frac{1}{2}\varepsilon_r^\top \varepsilon_r + \frac{1}{2}\varepsilon_M^\top \varepsilon_M \tag{74}$$

results in the following disturbance estimation of $w_r(t)$ and $w_e(t)$ in the form of least-squares gradient adaptive laws

$$\dot{\hat{w}}_r^\top = -\Gamma_{w_r} \frac{\partial J^\top}{\partial \hat{w}_r^\top} = -\Gamma_{w_r}\left(\varepsilon_r^\top + M_{w_r}\varepsilon_M^\top\right) \tag{75}$$

$$\dot{\hat{w}}_e^\top = -\Gamma_{w_e} \frac{\partial J^\top}{\partial \hat{w}_e^\top} = -\Gamma_{w_e} M_{w_e}\varepsilon_M^\top \tag{76}$$

Once the disturbance is estimated, we can proceed with the design of the multi-objective flight control.

C. Multi-Objective Flight Control

We formulate the Hamiltonian as

$$H = \frac{1}{2}\left(G_x x - G_r r\right)^\top Q \left(G_x x - G_r r\right) + \frac{1}{2}u^\top R u + \frac{1}{2}q_D\left(C_{D_x}x + C_{D_u}u + x^\top C_{D_{x^2}}x + x^\top C_{D_{xu}}u + u^\top C_{D_{u^2}}u\right)$$
$$+ \frac{1}{2}q_M\left(M_x x + M_u u + M_w w\right)^\top\left(M_x x + M_u u + M_w w\right) + \lambda^\top\left(Ax + Bu + w\right) \quad (77)$$

where $G_x = \text{diag}\,(F,I)$ and $G_r = \text{diag}\,(I,0)$.

The adjoint equation and optimal control are obtained as

$$\dot{\lambda} = -\frac{\partial H}{\partial x}^\top = -G_x^\top Q\left(G_x x - G_r r\right) - \frac{1}{2}q_D\left(C_{D_x}^\top + 2C_{D_{x^2}}^\top x + C_{D_{xu}}u\right) - q_M M_x^\top\left(M_x x + M_u u + M_w w\right) - A^\top\lambda \quad (78)$$

$$\frac{\partial H}{\partial u}^\top = Ru + \frac{1}{2}q_D\left(C_{D_u}^\top + C_{D_{xu}}^\top x + 2C_{D_{u^2}}^\top u\right) + q_M M_u^\top\left(M_x x + M_u u + M_w w\right) + B^\top\lambda = 0$$

$$\Rightarrow u = -\left(R + \frac{1}{2}q_D C_{D_{u^2}}^\top + q_M M_u^\top M_u\right)^{-1}\left(B^\top\lambda + \frac{1}{2}q_D C_{D_u}^\top + \frac{1}{2}q_D C_{D_{xu}}^\top x + q_M M_u^\top M_x x + q_M M_u^\top M_w w\right) \quad (79)$$

Let $\lambda\left(t\right) = W\left(t\right)x\left(t\right) + V\left(t\right)$. Then

$$\left(\dot{W} + W\bar{A} + \bar{A}^\top W - WB\bar{R}^{-1}B^\top W + \bar{Q}\right)x + \left(\bar{A}^\top - WB\bar{R}^{-1}B^\top\right)V + \dot{V} = G_x^\top QG_r r - \frac{1}{2}q_D C_{D_x}^\top$$
$$+ \frac{1}{2}q_D\left(WB + \frac{1}{2}q_D C_{D_{xu}} + q_M M_x^\top M_u\right)\bar{R}^{-1}C_{D_u}^\top - Ww - q_M M_x^\top M_w w$$
$$+ q_M\left(WB + \frac{1}{2}q_D C_{D_{xu}} + q_M M_x^\top M_u\right)\bar{R}^{-1}M_u^\top M_w w \quad (80)$$

where

$$\bar{R} = R + \frac{1}{2}q_D C_{D_{u^2}}^\top + q_M M_u^\top M_u \quad (81)$$

$$\bar{A} = A - \frac{1}{2}q_D B\bar{R}^{-1}C_{D_{xu}}^\top - q_M B\bar{R}^{-1}M_u^\top M_x \quad (82)$$

$$\bar{Q} = G_x^\top QG_x + q_D C_{D_{x^2}}^\top + q_M M_x^\top M_x - \left(\frac{1}{2}q_D C_{D_{xu}}^\top + q_M M_u^\top M_x\right)^\top\bar{R}^{-1}\left(\frac{1}{2}q_D C_{D_{xu}}^\top + q_M M_u^\top M_x\right) \quad (83)$$

We choose q_D and q_M appropriately to ensure $\bar{Q} > 0$.

For the infinite time-horizon optimal control, $\dot{W} = 0$ and $\dot{V} = 0$. Therefore, we obtain

$$W\bar{A} + \bar{A}^\top W - WB\bar{R}^{-1}B^\top W + \bar{Q} = 0 \quad (84)$$

$$V = V_0 + V_r r + V_w w \quad (85)$$

$$V_0 = \left(\bar{A}^\top - WB\bar{R}^{-1}B^\top\right)^{-1}\left[-\frac{1}{2}q_D C_{D_x}^\top + \frac{1}{2}q_D\left(WB + \frac{1}{2}q_D C_{D_{xu}} + q_M M_x^\top M_u\right)\bar{R}^{-1}C_{D_u}^\top\right] \quad (86)$$

$$V_r = \left(\bar{A}^\top - WB\bar{R}^{-1}B^\top\right)^{-1}G_x^\top QG_r \quad (87)$$

$$V_w = \left(\bar{A}^\top - WB\bar{R}^{-1}B^\top\right)^{-1}\left[-W - q_M M_x^\top M_w + q_M\left(WB + \frac{1}{2}q_D C_{D_{xu}} + q_M M_x^\top M_u\right)\bar{R}^{-1}M_u^\top M_w\right] \quad (88)$$

The multi-objective flight controller is expressed as

$$u = K_x\hat{x} + K_r r + K_w\hat{w} + \Lambda_0 \quad (89)$$

where

$$K_x = -\bar{R}^{-1}\left(B^\top W + \frac{1}{2}q_D C_{D_{xu}}^\top + q_M M_u^\top M_x\right) \quad (90)$$

$$K_r = -\bar{R}^{-1}B^\top V_r \quad (91)$$

$$K_w = -\bar{R}^{-1}\left(B^\top V_w + q_M M_u^\top M_w\right) \quad (92)$$

$$\Lambda_0 = -\bar{R}^{-1}\left(B^\top V_0 + \frac{1}{2}q_D C_{D_u}^\top\right) \quad (93)$$

American Institute of Aeronautics and Astronautics

D. VCCTEF Virtual Control Variables

All the control surfaces are not entirely independent in their motions due to the physical constraints imposed by the elastomer transition material. This material has certain displacement and rate limits. Thus, the control surfaces will have relative deflection and rate limits imposed on them. These limits are not the position and rate limits that flight control actuators are normally subjected to. Thus, these relative constraints can cause challenges in a control design of this system.

Consider the following relative constraints

$$|\delta_{i+1} - \delta_i| \leq \Delta\delta \tag{94}$$

$$\left|\dot{\delta}_{i+1} - \dot{\delta}_i\right| \leq \Delta\dot{\delta} \tag{95}$$

where $i = 1, 2, \ldots, m$ is the index of each flap section and m is the number of spanwise flap sections of the VCCTEF per wing.

For the VCCTEF design, the relative motion between any adjacent flap sections is allowed to be within $2°$. The rate constraint imposed by the elastomer transition material is not yet defined and thus is not considered.

To address the relative deflection limit, a concept of virtual control has been introduced.[6] The control surface deflections are described by a shape function. This shape function can be any reasonable shape function with a smooth and gradual slope. Suppose the ideal continuous trailing edge of the VCCTEF is mathematically smooth and can be described by a Fourier sine series as follows:

$$\delta^*(x) = A_0 + \sum_{n=1}^{N} A_n \sin \frac{n\pi x}{L} \tag{96}$$

where $\delta^*(x)$ is a theoretical VCCTEF deflection and N is the number of terms in the Fourier sine series.

In reality, the trailing edge of the VCCTEF is only stepwise continuous due to the physical implementation. Therefore, the actual VCCTEF deflection is a stepwise linear approximation of the theoretical VCCTEF deflection. Thus,

$$\delta_i = A_0 + \sum_{n=1}^{N} A_n \sin \frac{(i-1)n\pi}{N-1} \tag{97}$$

where i is the flap index.

Note that A_0 is the constant flap deflection which is needed to provide flexibility for multi-objective flight control, especially for drag reduction control. The constant flap deflection at the wing tip can be used to create a zero lift condition to minimize tip vortices. The quantities A_n, $n = 0, 1, \ldots, N$ can be viewed as virtual control variables. The virtual control variables are then used in a flight control design to determine their command settings. Then, the actual VCCTEF deflection command δ_c can be computed from the virtual control commands A_n. Since Eq. (97) is linear in the virtual commands, a transformation matrix that relates the physical control variables to the virtual control variables can be constructed straightforwardly using the partial derivatives with respect to the virtual control variables.

E. Simulations

A coupled ASE longitudinal dynamic model of the flexible wing GTM is constructed. The wing stiffness is reduced by 50% from the baseline stiffness. The model has 5 rigid aircraft states in the longitudinal direction, 10 aeroelastic modes with 2 elastic states and 4 aerodynamic lag states per mode, two rigid aircraft flight control inputs; namely, the elevator and engine throttle each with one actuator state, and 16 VCCTEF inputs to the outermost chordwise flap segments with 2 actuator states and 4 aerodynamic lag states per flap segment. Thus, the model has a total of 179 states and 18 control variables. The model includes an aerodynamic model that computes the aircraft lift and drag coefficients as well as a structural model that computes the wing root bending moment and wing acceleration.

Generally, the aeroelastic state vectors are not accessible, but can be estimated by an observer design, which is a standard control practice. It is possible to reconstruct the aeroelastic deflections from limited sensor measurements by the Luenberger state observer design. Assuming that the aeroelastic states can be reconstructed by an observer design for feedback control and that the estimation error is sufficiently small, a flight control task can be designed with the estimated aeroelastic states as feedback state variables. The linear quadratic gaussian (LQG) is a standard technique for control design of systems with output or partial state information. A state observer is constructed using the Kalman filter optimal estimation method.

American Institute of Aeronautics and Astronautics

The Kalman filter receives measurements from eight accelerometers.[7] These vertically oriented accelerometers are placed in pairs at mid-span and the wing tips. At each location, one accelerometer is placed forward of the elastic axis and one is placed aft of the elastic axis. The accelerometer locations on the left wing are indicated by the four red dots in Fig. 10.[7] By placing the accelerometers in pairs forward and aft of the elastic axis, it is possible to not only measure the vertical acceleration of the wing section, but also the angular acceleration, i.e. twist acceleration. Care must be exercised in the accelerometer signal conditioning to ensure synchronous sampling to prevent a phase shift among the accelerometer signals which could affect the control objective.
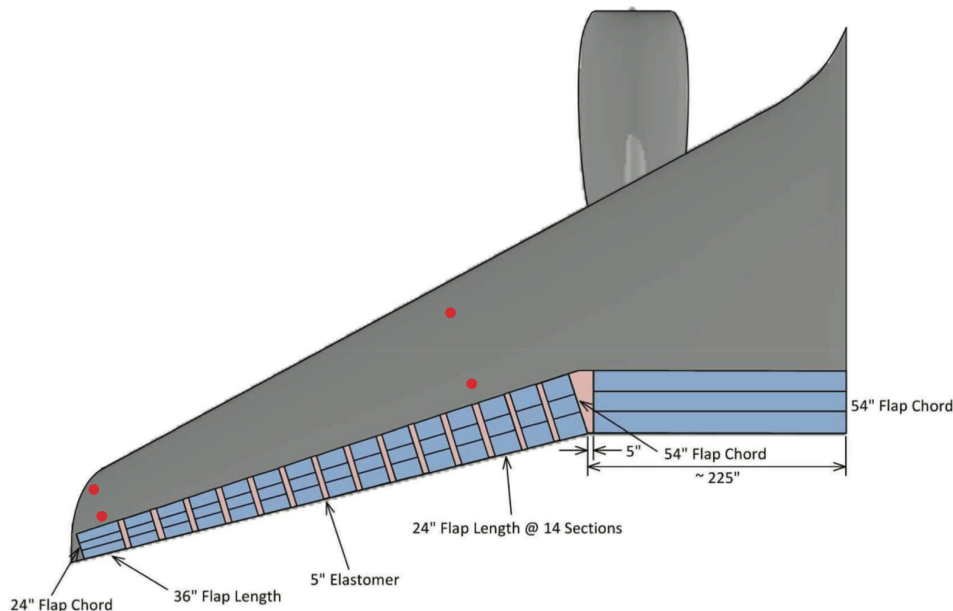
Figure 10. Accelerometer Locations

Before the accelerometer measurements can be used in the Kalman filter, they need to pass through a low-pass filter. There are two reasons why this is necessary. Firstly, measurement noise needs to be filtered out. Secondly, contributions of high frequency modes that are not maintained in the reduced-order model may negatively affect the state estimation. While these high frequency modes do not reach large amplitudes, they do contribute significantly to the accelerometer output, which leads to a mismatch between the measured output and the predicted output in the design the Kalman filter. Therefore, the cut-off frequency of the low-pass filter should be chosen with the maximum frequency of the elastic modes in the reduced-order model in mind. In order to minimize the delay of the measurement signal by limiting the phase shift due to the low-pass filter, a Bessel filter is generally suitable for low-pass filtering.[7]

A flight path angle control is designed with the aeroelastic mode suppression and drag minimization. The flight condition is Mach 0.797 at an altitude of 36,000 ft. Figure 11 shows the response of the aircraft to the flight path angle control with the aeroelastic mode suppression and drag minimization. The aeroelastic mode suppression uses a weighting matrix $Q_e = 50$ and the drag minimization uses a weighting coefficient $q_D = 5 \times 10^4$. The flight path angle response with the aeroelastic mode suppression and drag minimization is well-behaved and tracks the command very well. With the rigid aircraft controller alone, the aircraft angle of attack, pitch rate, and pitch angle exhibit large transients which are undesirable.
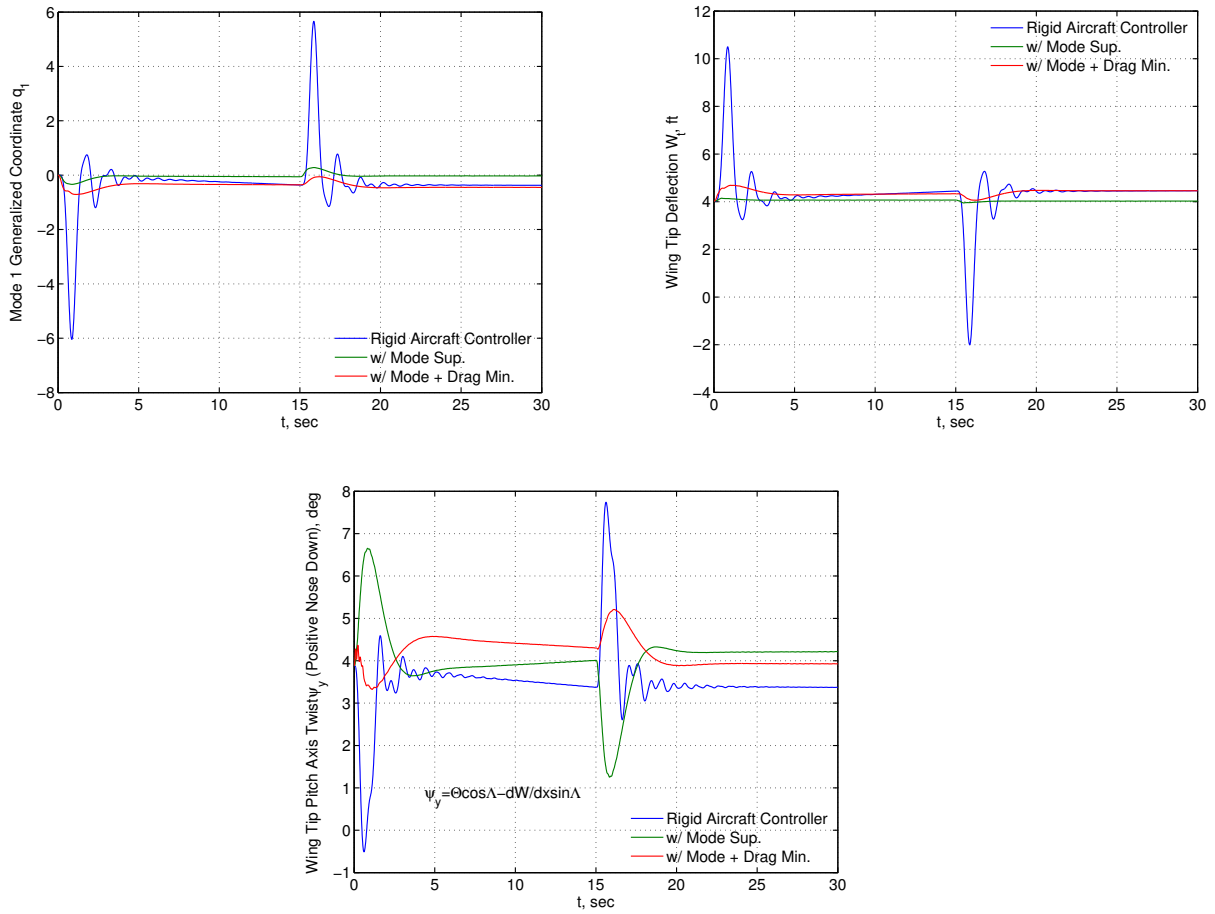
American Institute of Aeronautics and Astronautics
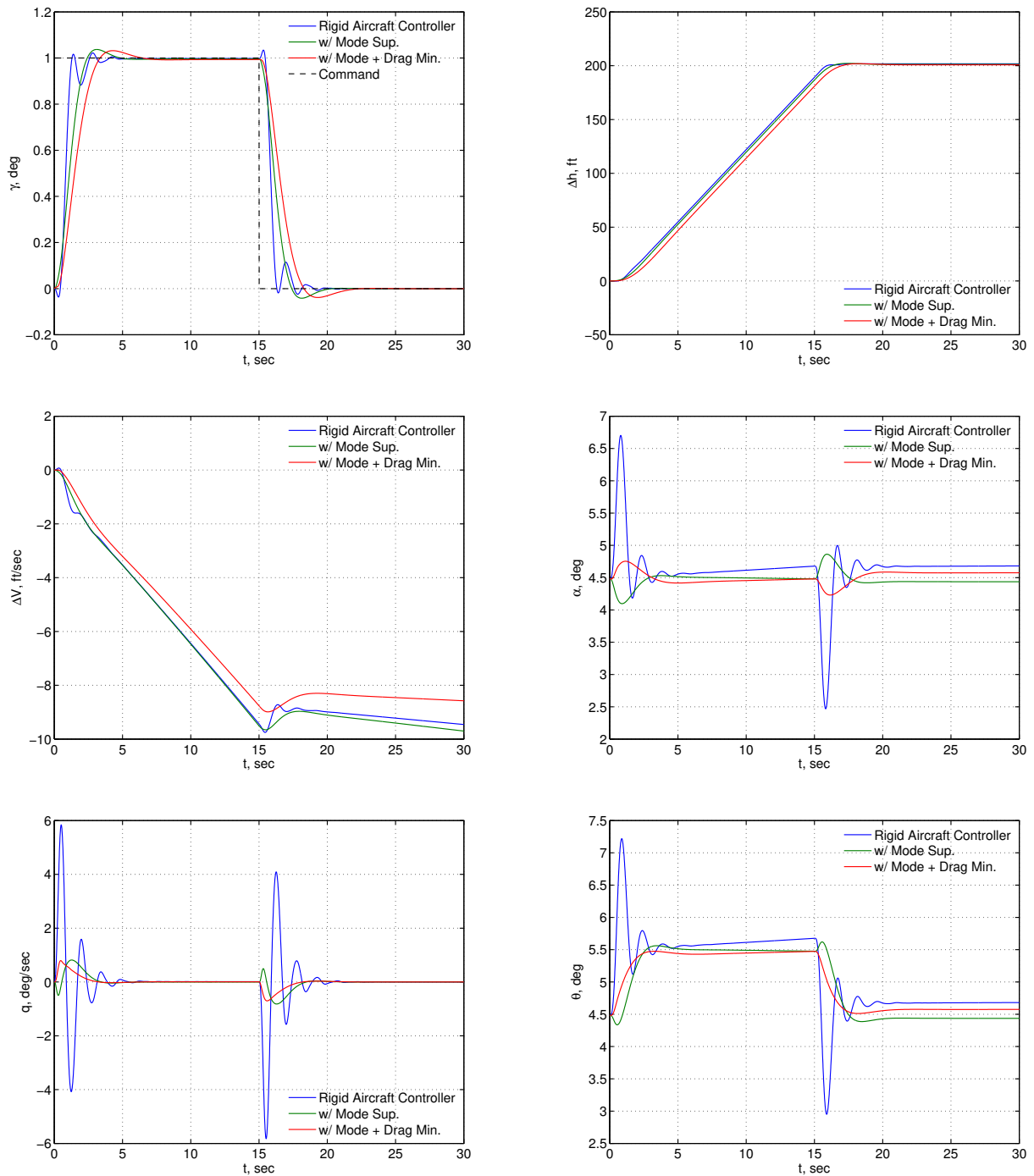
Figure 11. Rigid Aircraft Response to Multi-Objective Flight Control with Mode Suppression and Drag Minimization

Figure 12 shows the response of the flexible wing. With the rigid aircraft controller alone, the wing tip deflection and wing tip pitch axis twist are very excessive. With the aeroelastic mode suppression, the aeroelastic deflections are substantially reduced. Thus, this illustrates the importance of the aeroelastic mode suppression in a flight control design for flexible aircraft. Without aeroelastic mode suppression, the wing aeroelastic response can cause the rigid aircraft to behave unpredictably.

American Institute of Aeronautics and Astronautics

Figure 12. Flexible Wing Response to Multi-Objective Flight Control with Mode Suppression and Drag Minimization

Figure 13 shows the control surface deflections of the elevator and the VCCTEF numbered from 1 at the wing root to 16 at the wing tip. With the rigid aircraft controller alone, the elevator deflection is quite excessive, but becomes much more reasonable with the aeroelastic mode suppression and drag minimization. The deflections of the outermost chordwise flap segments of the VCCTEF range from $-11.2°$ to $9.5°$ for the aeroelastic mode suppression and from $-13.8°$ to $6.6°$ for the aeroelastic mode suppression plus drag minimization. The deflections are well-behaved without any large transients. Note that the VCCTEF deflections for the rigid aircraft controller alone are not zero. This is because the flaps are compliant and respond to the hinge moments generated by the rigid aircraft states and wing elastic states.

American Institute of Aeronautics and Astronautics
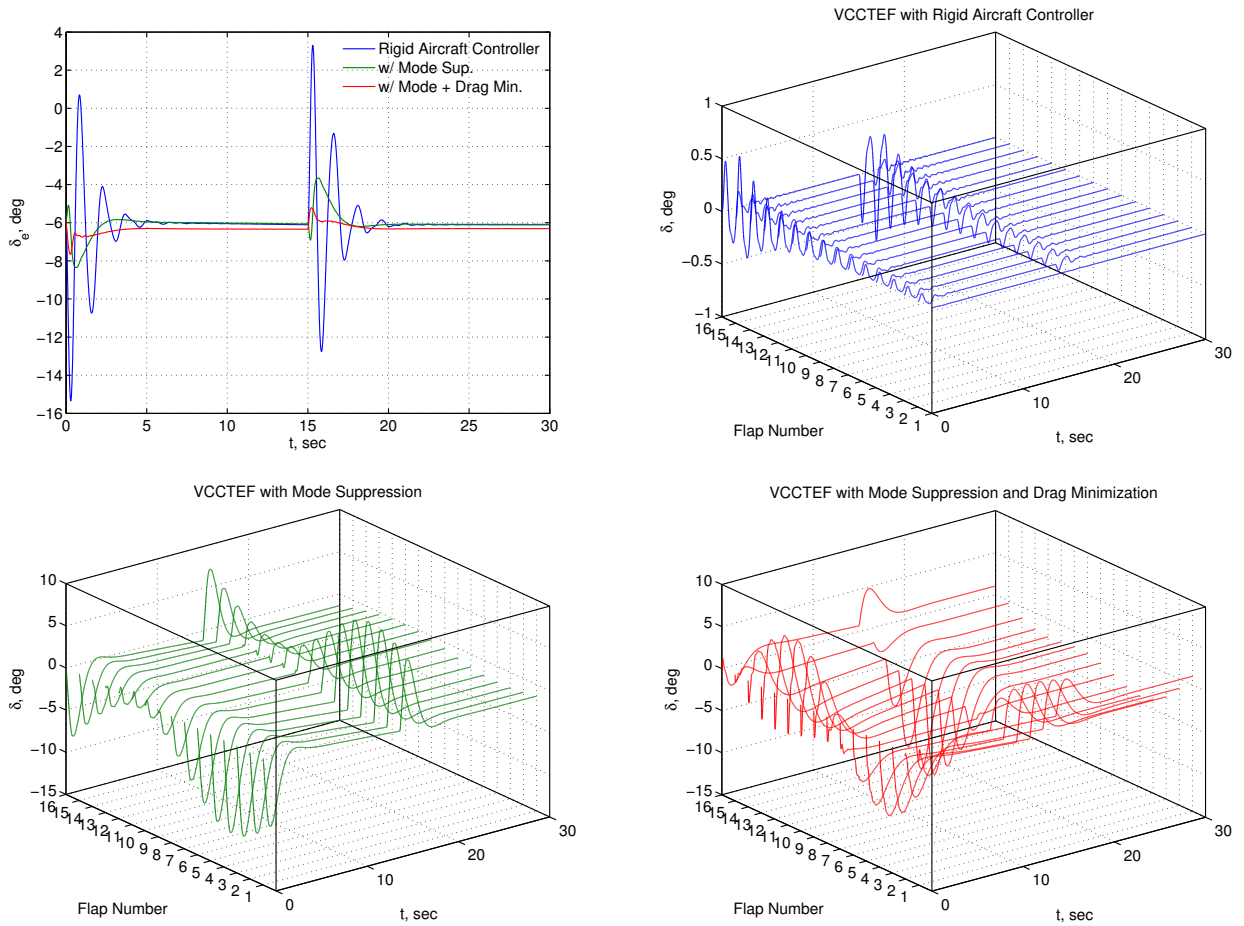
Figure 13. Control Surface Deflections for Multi-Objective Flight Control with Mode Suppression and Drag Minimization

Figure 14 shows the lift and drag coefficients of the aircraft due to the flight path angle control with the aeroelastic mode suppression and drag minimization. With the rigid aircraft controller alone, the lift coefficient exhibits large initial transients. The drag coefficient is generally smaller with than without the drag minimization as expected. The response of the aircraft lift-to-drag ratio is also shown in Fig. 14. At the final time when the flight angle has settled to its steady state value, the L/D value shows an improvement of about 1.25%. Note that this figure of merit is sensitive to the selection of the weighting matrix Q_e and weighting coefficient q_D. In general, reducing the weighting matrix Q_e can result in a better L/D value, but the aeroelastic mode suppression is less effective. A trade analysis can be performed to determine a good compromised design between the aeroelastic mode suppression and drag minimization.

Table 3 shows the results of a sensitivity analysis of the drag minimization without the aeroelastic mode suppression. As q_D increases, the L/D improvement increases along with the increase in the VCCTEF deflections. For $q_D = 5 \times 10^4$, a 7% L/D improvement can be attained. As Q_e increases, the L/D improvement becomes smaller. For the simulations, with $Q_e = 50$ and $q_D = 5 \times 10^4$, the L/D improvement is only 1.25%. It is possible to use a smaller weight matrix Q_e to achieve a reasonable aeroelastic mode suppression and a larger L/D improvement.
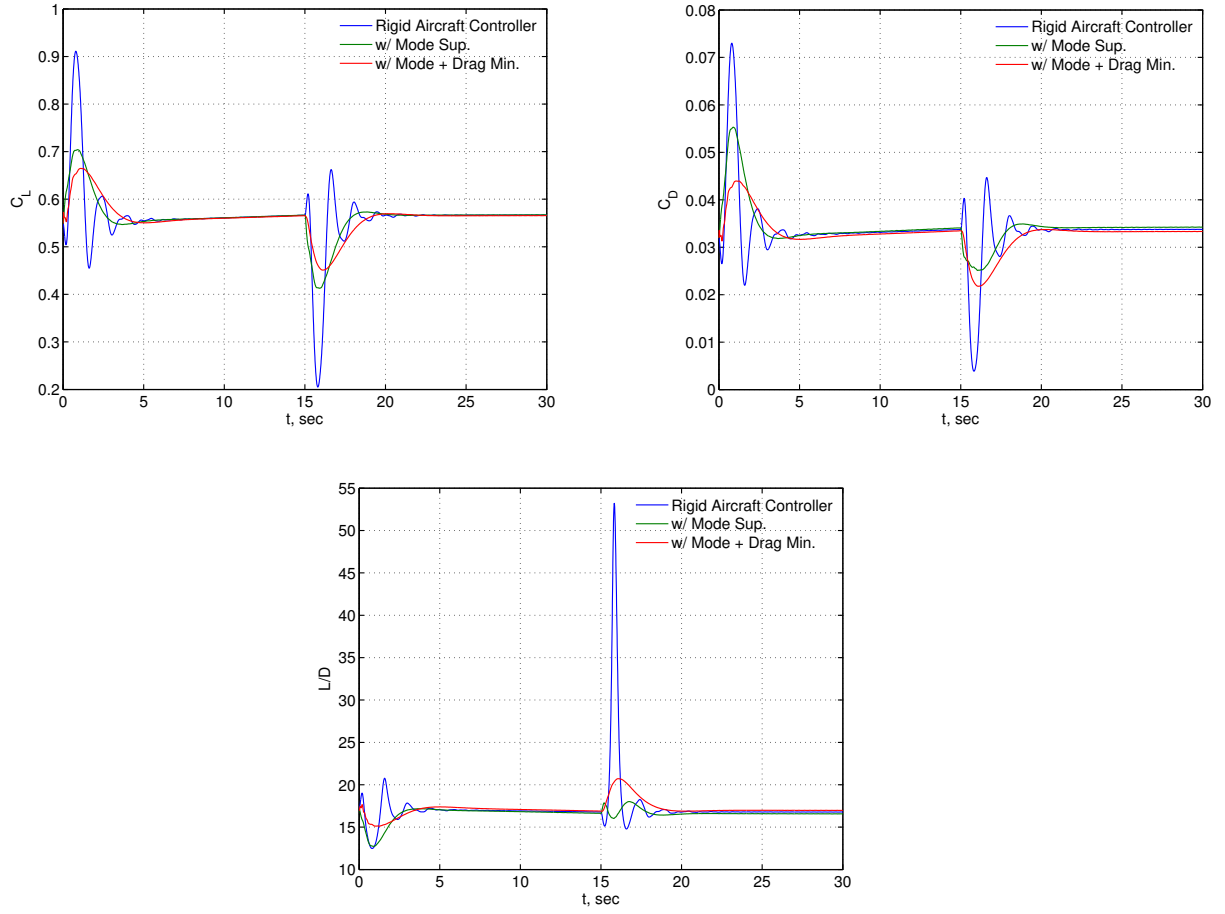
American Institute of Aeronautics and Astronautics

Figure 14. Aerodynamic Performance Response to Multi-Objective Flight Control with Mode Suppression and Drag Minimization

$q_D \times 10^3$	$\left.\left\|\frac{\gamma - \gamma_c}{\gamma_c}\right\|\right\|_{t=15}$, %	$\alpha\|_{t=30}$	$\|\Delta \delta_{e,max}\|$	$\|\delta_{max}\|$	$\left.\frac{L}{D}\right\|_{t=30}$	$\left.\frac{L}{D}\right\|_{t=30}$ Improvement, %
0	0.2061	4.6816°	9.4109°	0.5756°	16.7797	0
5	0.2827	4.6600°	4.1390°	5.6057°	16.8933	0.6782
10	0.3356	4.6885°	3.5747°	4.7044°	17.0276	1.4871
15	0.3733	4.7121°	3.2969°	5.7423°	17.1500	2.2077
20	0.3998	4.7339°	3.1545°	7.7536°	17.2728	2.9395
25	0.4272	4.7542°	3.0932°	9.7121°	17.3898	3.6367
30	0.4419	4.7739°	3.0858°	11.6059°	17.5113	4.3609
35	0.4593	4.7928°	3.1117°	13.4628°	17.6272	5.0519
40	0.4696	4.8111°	3.1598°	15.2157°	17.7367	5.7044
45	0.4780	4.8287°	3.2215°	16.9191°	17.8511	6.3862
50	0.4900	4.8459°	3.2964°	18.5546°	17.9600	7.0350

Table 3. Sensitivity Analysis of Drag Minimization without Mode Suppression

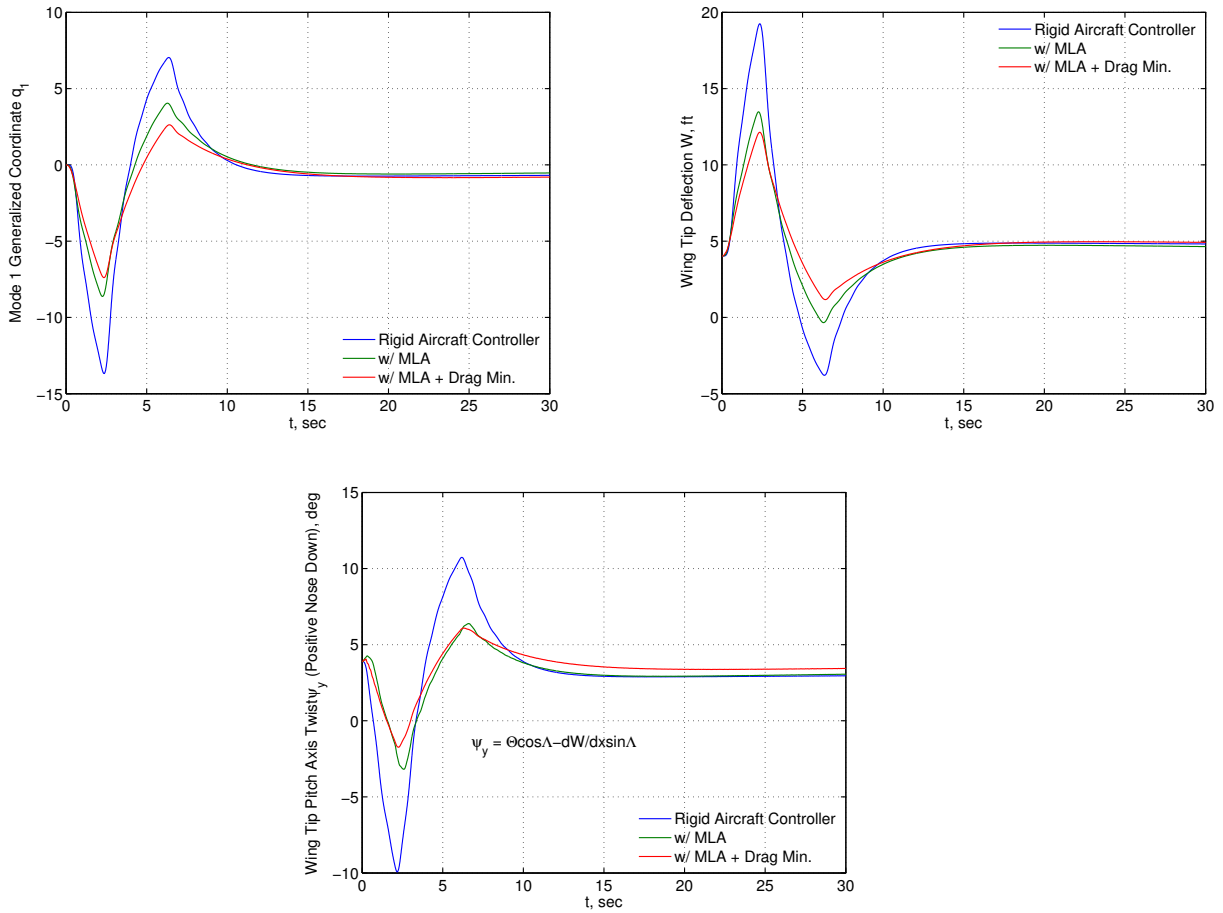American Institute of Aeronautics and Astronautics
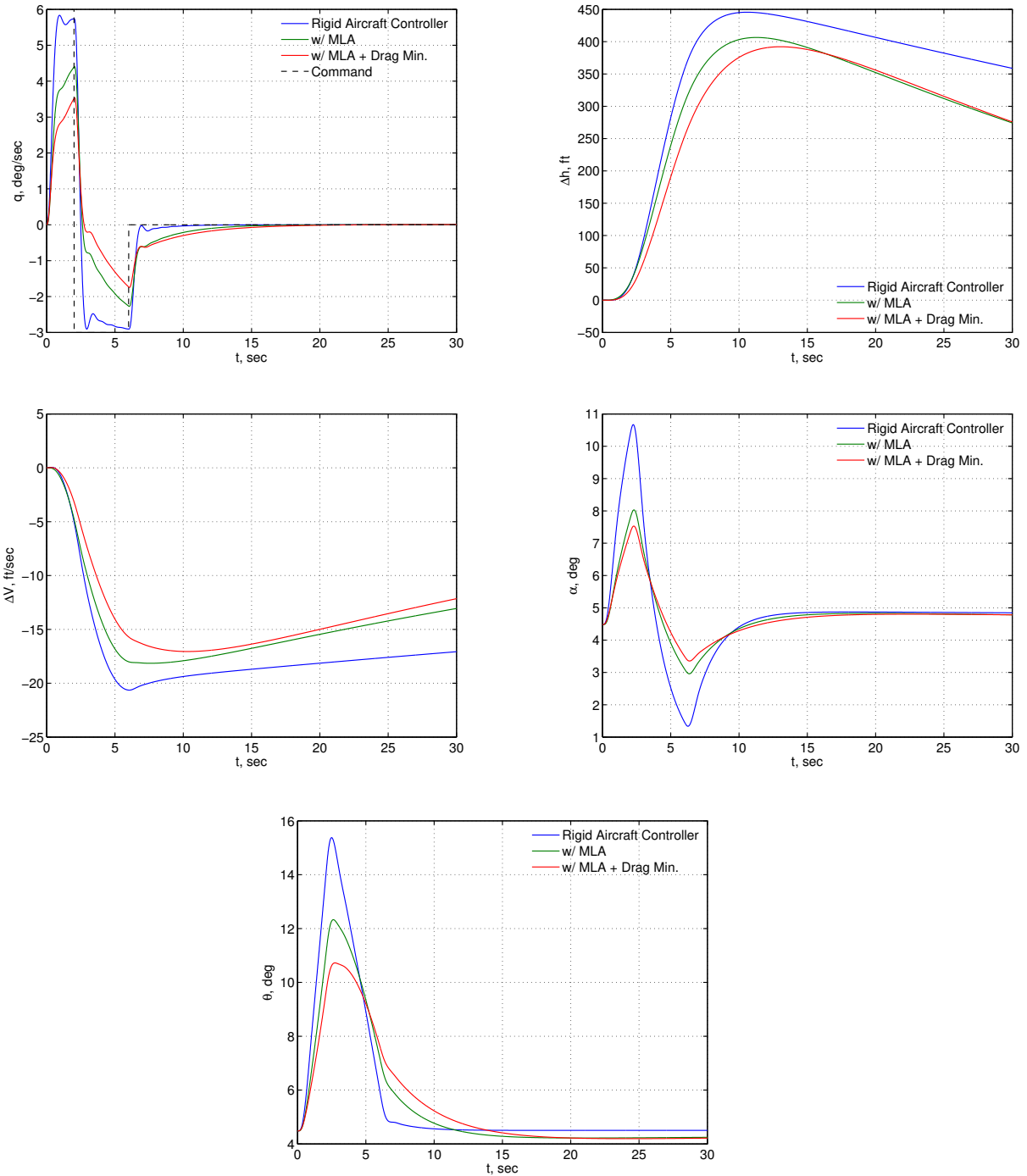
Figure 15. Rigid Aircraft Response to Multi-Objective Flight Control with Maneuver Load Alleviation (MLA) and Drag Minimization

A pitch rate control is designed for the maneuver load alleviation and drag minimization. The flight condition is at Mach 0.797 and an altitude of 36,000 ft. The aircraft performs a sharp 2.5-g pull-up. The maneuver load alleviation uses a weighting coefficient $q_M = 6 \times 10^{-12}$ and the drag minimization uses a weighting coefficient $q_D = 2.5 \times 10^3$. Figure 15 shows the response of the aircraft to the multi-objective flight control with the maneuver load alleviation and drag minimization. With the rigid aircraft controller alone, the pitch rate response increases to $5.8°$/sec. The angle of attack also increases sharply to $10.7°$ which is near stall. With the maneuver load alleviation, the pitch rate response is

American Institute of Aeronautics and Astronautics

curtailed to 4.4°/sec. The angle of attack is then brought down to about 8.0°. When the drag minimization is included, the pitch rate response is further reduced to 3.5°/sec and the angle of attack comes down to 7.5°. Because the maneuver load alleviation is designed to reduce to wing root bending moment, the tracking of the pitch rate command is poor, but in exchange the wing root bending moment is reduced to ensure that the structural load limit is conformed.

Figure 16 shows the response of the flexible wing. With the rigid aircraft controller alone, the aeroelastic deflections of the wing are highly excessive. The wing tip deflection is well over 19 ft which most likely invalidates the small deflection assumption in the linear finite-finite element model. The wing tip pitch axis twist of more than 10° with the rigid aircraft controller alone is also extremely large. With the maneuver load alleviation, the aeroelastic deflections are brought down to about 13 ft and 6° at the wing tip. By including the drag minimization, the wing tip deflection decreases further to about 12 ft.

Figure 16. **Flexible Wing Response to Multi-Objective Flight Control with Maneuver Load Alleviation (MLA) and Drag Minimization**

Figure 17 shows the control surface deflections of the elevator and the VCCTEF. With the rigid aircraft controller alone, the largest elevator deflection is at −15° with the rigid aircraft controller alone. With the maneuver load alleviation, the elevator deflection is reduced to −13.4°. By including the drag minimization, the elevator deflection further decreases to −11.9°. The deflections of the outermost chordwise flap segments of the VCCTEF range from −10.1° to 5.6° for the maneuver load alleviation and from −6.0° to 3.9° for the maneuver load alleviation plus drag minimization. The deflections are well-behaved without any large transients.
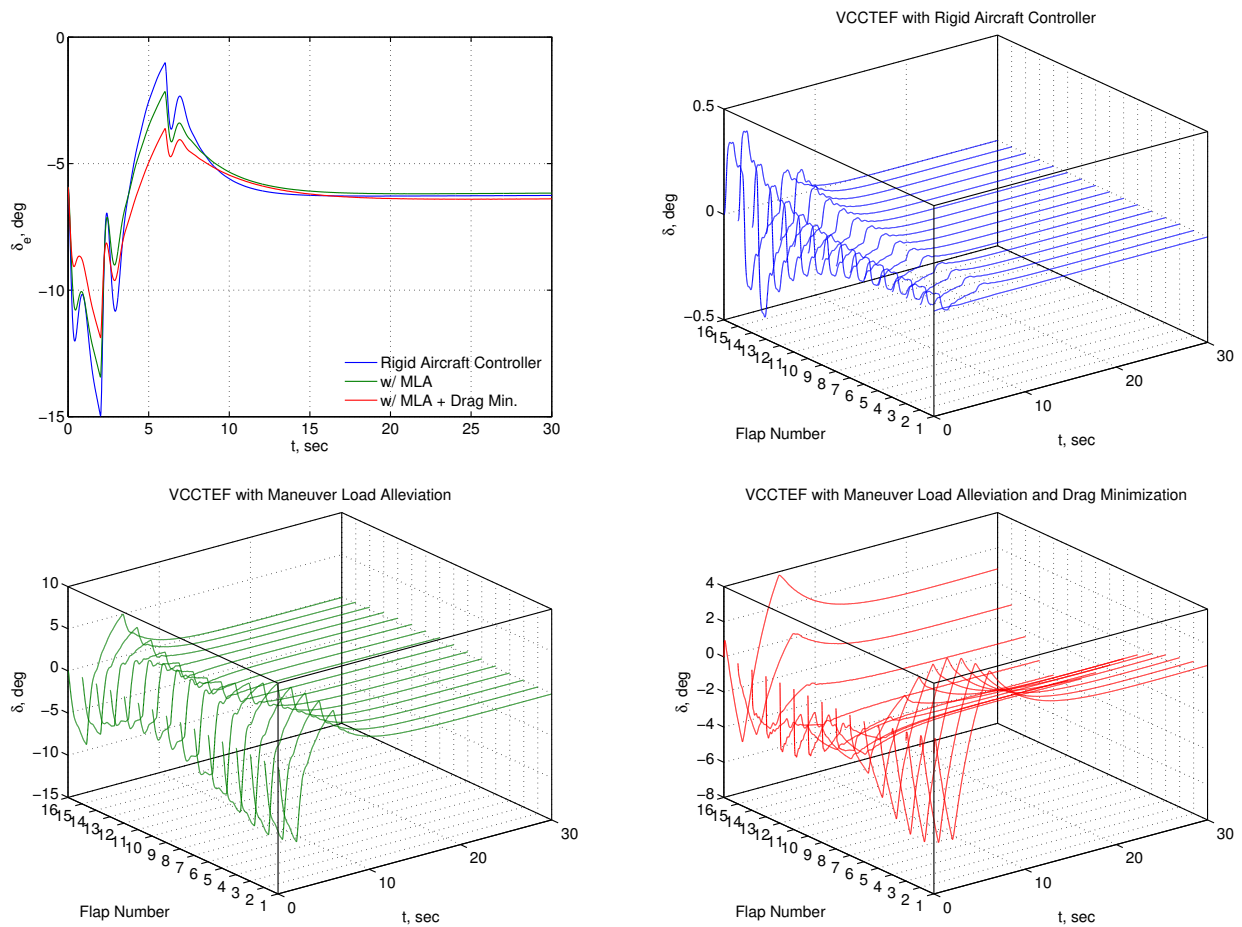
Figure 17. Control Surface Deflections for Multi-Objective Flight Control with Maneuver Load Alleviation (MLA) and Drag Minimization

Figure 18 shows the lift and drag coefficients of the aircraft and the wing root bending moment response due to the pitch rate control with the maneuver load alleviation and drag minimization. With the rigid aircraft controller alone, the lift coefficient increases rapidly to a value corresponding to a load factor of 2.68 which would exceed the typical design load factor of 2.5. With the maneuver load alleviation, the load factor is reduced to about 2.26. With the inclusion of the drag minimization, the load factor is further reduced to about 2.03. Thus, the maneuver load alleviation reduces the load factor by up to 24% with the drag minimization. The wing root bending moments with the three controllers are 5.03×10^6 ft-lb, 3.66×10^6 ft-lb, and 3.27×10^6 ft-lb corresponding to the load factor of 2.68, 2.26, and 2.03, respectively. Thus, the maneuver load alleviation reduces the wing root bending moment by about 27% without and 35% with the drag minimization.

The response of the aircraft L/D is also shown in Fig. 18. At the final time when the flight angle has settled to its steady state value, the L/D value shows an improvement of about 2.3%. Note that this figure of merit is sensitive to the selection of the weighting coefficients q_M and q_D. In general, increasing the weighting coefficient q_D can result in a better L/D value as well as a reduced wing root bending moment. A trade analysis can be performed to determine a good compromised design between the maneuver load alleviation and drag minimization.

Table 4 shows the results of a sensitivity analysis of the maneuver load alleviation without the drag minimization. As q_M increases, the load factor and wing root bending moment both decrease along with the increase in the VCCTEF deflections.

American Institute of Aeronautics and Astronautics
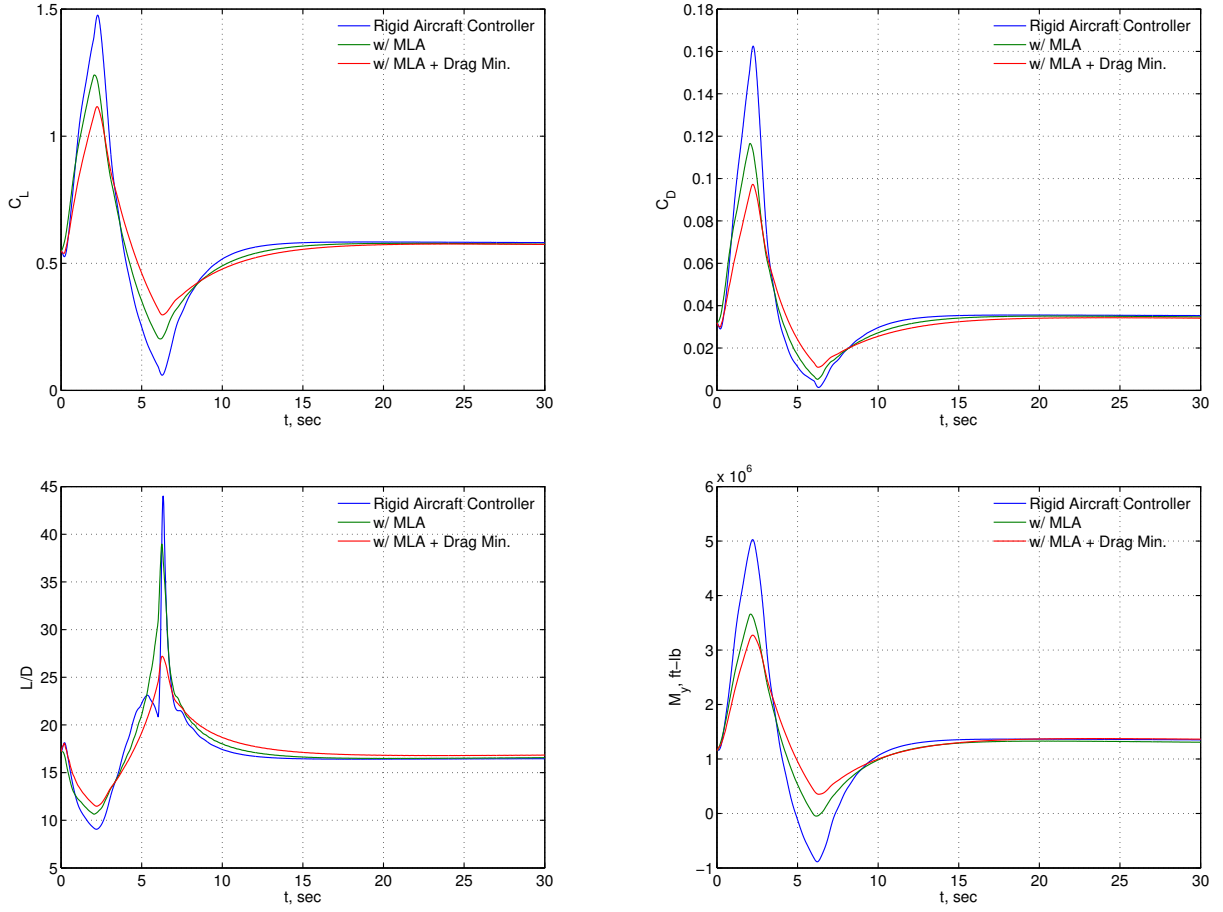
Figure 18. Aerodynamic Performance and Wing Root Bending Moment Responses to Multi-Objective Flight Control with Maneuver Load Alleviation (MLA) and Drag Minimization

$q_M \times 10^{-12}$	$\left\|\frac{q - q_c}{q_c}\right\|_{t=2}, \%$	n_{max}	$\|\Delta \delta_{e,max}\|$	$\|\delta_{max}\|$	$\|M_{y,max}\| \times 10^6$ ft-lb	M_y Reduction, %
0	4.3606	2.6782	4.9142°	0.4915°	5.0265	0
1	7.4266	2.5781	4.6135°	1.7116°	4.7667	5.1703
2	12.8159	2.4591	4.3087°	3.5025°	4.4291	11.8862
3	17.1426	2.3825	4.1067°	5.3271°	4.1753	16.9346
4	20.7869	2.3285	3.9635°	7.0830°	3.9742	20.9357
5	23.9441	2.2909	3.8559°	8.6781°	3.8089	24.2238
6	26.7497	2.2633	3.7711°	10.1296°	3.6687	27.0136

Table 4. Sensitivity Analysis of Maneuver Load Alleviation without Drag Minimization

In multi-objective optimization, different objectives can compete with one another, thereby resulting in a compromised solution. A Pareto frontier multi-objective analysis is performed to understand the trade space of the competing maneuver load alleviation and drag minimization objectives in the multi-objective flight control design.
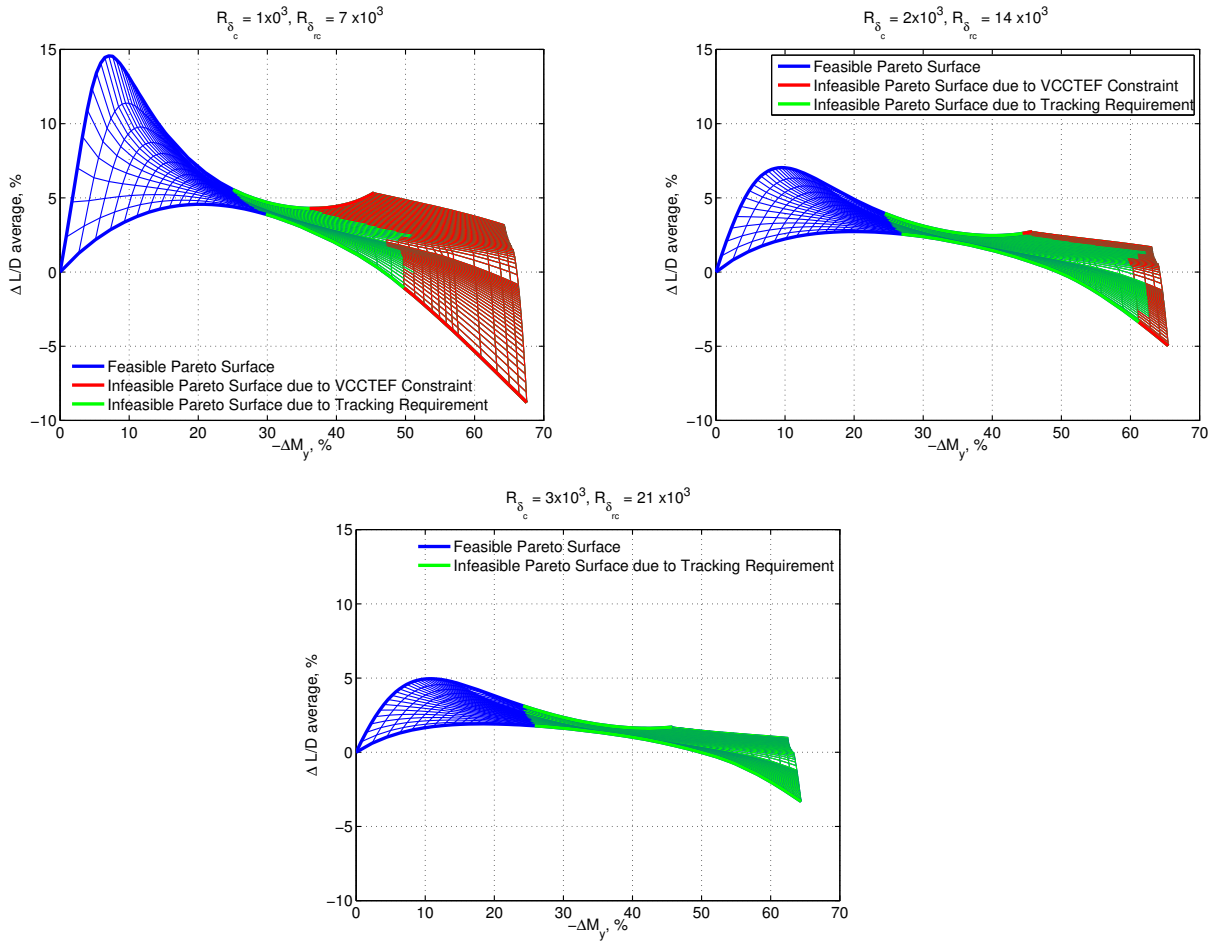
Figure 19 shows three different design trade spaces for different control weighting matrices R_{δ_c} for the VCCTEF and $R_{\delta_{rc}}$ for the elevator. For the first design with $R_{\delta_c} = 1 \times 10^3$ and $R_{\delta_{rc}} = 7 \times 10^3$, the design trade space for q_M

American Institute of Aeronautics and Astronautics

and q_D is the entire rectangular region of $q_M \leq 10 \times 10^{-10}$ and $q_D \leq 40 \times 10^4$. When the VCCTEF relative deflection constraint of $2°$ is applied, the design trade space is reduced to the green dot subset which limits q_M to 7×10^{-10} and q_D to 16×10^4. If a pitch rate tracking constraint is imposed on the control design to not exceed 30% of the pitch rate command at 2 sec, then the feasible design trade space is further reduced to the blue dot subset with $q_M \leq 2 \times 10^{-10}$ and $q_D \leq 6 \times 10^4$. Increasing the weighting matrices R_{δ_c} and $R_{\delta_{rc}}$ enlarges the feasible design trade space that satisfies the VCCTEF relative deflection constraint but does not change the feasible design trade space that satisfies both the constraints.
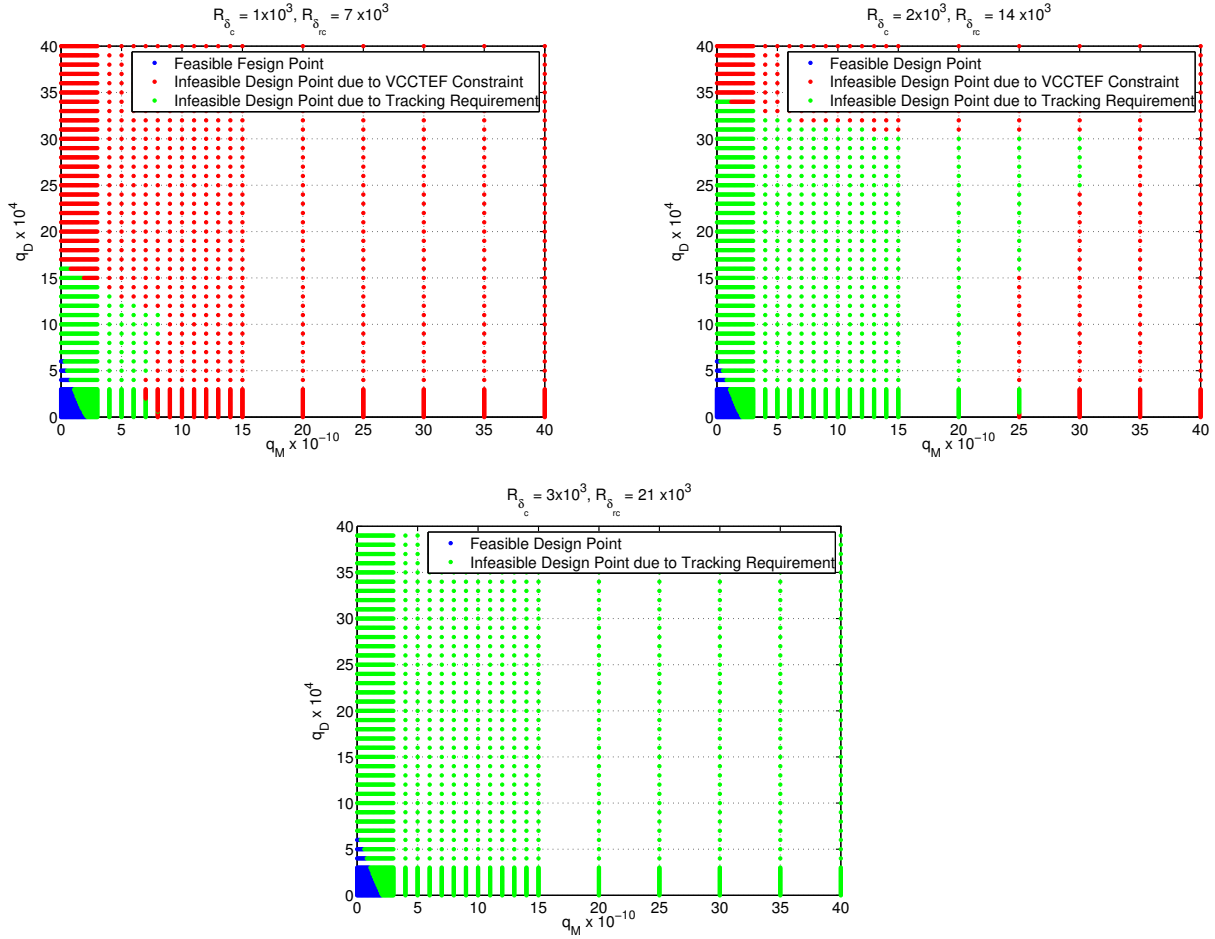
Figure 19. Multi-Objective Flight Control Design Trade Space for Maneuver Load Alleviation and Drag Minimization

Figure 20 shows the Pareto surfaces of the three design trade spaces in Fig. 19. For the first design with $R_{\delta_c} = 1 \times 10^3$ and $R_{\delta_{rc}} = 7 \times 10^3$, the maximum wing root bending moment reduction is 67.6% and the maximum L/D improvement is 14.6% without any constraints imposed on the control design. The VCCTEF relative deflection constraint significantly reduces the maximum wing root bending moment reduction to 51.2%. With the pitch rate tracking constraint, the maximum wing root bending moment reduction decreases to 29.8%. The maximum L/D improvement is not affected by both the constraints. As the weighting matrices R_{δ_c} and $R_{\delta_{rc}}$ increase, the maximum L/D improvement decreases to 9.5% for $R_{\delta_c} = 2 \times 10^3$ and $R_{\delta_{rc}} = 14 \times 10^3$ and 5.0% for $R_{\delta_c} = 3 \times 10^3$ and $R_{\delta_{rc}} = 21 \times 10^3$. For both of these design trade spaces, the maximum wing root bending moment reduction are about the same at 26.9% for the second design trade space and 25.9% for the third design trade space. Examining the Pareto surfaces for the three design trade spaces, the first design trade space provides a better compromised control design with the maximum wing root bending moment reduction of 25.0% and the maximum drag reduction of 5.6%.

American Institute of Aeronautics and Astronautics

$R_{\delta_c} = 1 \times 0^3$, $R_{\delta_{rc}} = 7 \times 10^3$

$R_{\delta_c} = 2 \times 10^3$, $R_{\delta_{rc}} = 14 \times 10^3$

$R_{\delta_c} = 3 \times 10^3$, $R_{\delta_{rc}} = 21 \times 10^3$

Figure 20. Multi-Objective Flight Control Pareto Surface for Maneuver Load Alleviation and Drag Minimization

V. Conclusions

This paper presents a multi-objective flight control method for drag minimization, aeroelastic mode suppression, and maneuver load alleviation. The present study is an extension of the previous development of multi-objective flight control for flexible aircraft equipped with multi-functional flight control surfaces such as the Variable Camber Continuous Trailing Edge Flap system. The multi-objective flight control addresses multiple competing needs in a flight control design to achieve the goals of maximizing the aerodynamic performance of an aircraft, minimizing structural loads and aeroelastic response of the wing structure, and tracking a pilot command. The aerodynamic performance and structural response objectives are integrated into the traditional cost function of linear quadratic optimal control to synthesize a multi-objective flight control design. The resulting optimal control laws depend on the drag and structural sensitivity parameters. Gust load alleviation is also developed based on gust disturbance estimation. Simulations of the multi-objective flight control are conducted for a flexible wing Generic Transport Model. The results demonstrate the effectiveness of the multi-objective flight control in achieving aeroelastic mode suppression, drag minimization, and maneuver load alleviation while tracking a pilot command. A Pareto trade study is conducted to examine the design trade space in the multi-objective flight control for maneuver load alleviation and drag minimization. In a multi-objective flight control, different objectives can be competing with one another. A multi-objective flight control design therefore requires identifying an optimal solution that represents the best compromise among all the competing objectives. By examining the Pareto surfaces for different design trade spaces, an optimal compromised solution can be identified for the maneuver load alleviation and drag minimization.

American Institute of Aeronautics and Astronautics

Acknowledgment

References

[1]Nguyen, N., "Elastically Shaped Future Air Vehicle Concept," NASA Innovation Fund Award 2010 Report, October 2010, Submitted to NASA Innovative Partnerships Program, http://ntrs.nasa.gov/archive/nasa/casi.ntrs.nasa.gov/20110023698.pdf

[2]Nguyen, N., Trinh, K., Reynolds, K., Kless, J., Aftosmis, M., Urnes, J., and Ippolito, C., "Elastically Shaped Wing Optimization and Aircraft Concept for Improved Cruise Efficiency," AIAA Aerospace Sciences Meeting, AIAA-2013-0141, January 2013.

[3]Boeing Report No. 2012X0015, "Development of Variable Camber Continuous Trailing Edge Flap System," October 4, 2012.

[4]Urnes, J., Nguyen, N., Ippolito, C., Totah, J., Trinh, K., and Ting, E., "A Mission Adaptive Variable Camber Flap Control System to Optimize High Lift and Cruise Lift to Drag Ratios of Future N+3 Transport Aircraft," AIAA Aerospace Sciences Meeting, AIAA-2013-0214, January 2013.

[5]Nguyen, N., Ting, E., Nguyen, D., Trinh, K., "Flutter Analysis of Mission-Adaptive Wing with Variable Camber Continuous Trailing Edge Flap," 55th AIAA/ASME/ASCE/AHS/ASC Structures, Structural Dynamics, and Materials Conference, AIAA-2014-0839, January 2014.

[6]Nguyen, N. and Urnes, J., "Aeroelastic Modeling of Elastically Shaped Aircraft Concept via Wing Shaping Control for Drag Reduction," AIAA Atmospheric Flight Mechanics Conference, AIAA-2012-4642, August 2012.

[7]Nguyen, N. and Tal, E., "A Multi-Objective Flight Control Approach for Performance Adaptive Aeroelastic Wing," 56th AIAA/ASME/ASCE/AHS/SC Structures, Structural Dynamics, and Materials Conference, AIAA-2015-1843, January 2015.

[8]Nguyen, N., Lebofsky, S., Ting, E., Kaul, U., Chaparro, D., and Urnes, J., "Development of Variable Camber Continuous Trailing Edge Flap for Performance Adaptive Aeroelastic Wing," SAE AeroTech Congress & Exhibition, 15ATC-0250 / 2015-01-2565, September 2015.

[9]Lebofsky, S., Ting, E., and Nguyen, N., "Multidisciplinary Drag Optimization of Reduced Stiffness Flexible Wing Aircraft With Variable Camber Continuous Trailing Edge Flap," 56th AIAA/ASME/ASCE/AHS/ASC Structures, Structural Dynamics, and Materials Conference, AIAA-2015-1408, January 2015.

[10]Nguyen, N, Precup, N., Urnes, J., Nelson, C., Lebofsky, S., Ting, E., and Livne, E., "Experimental Investigation of a Flexible Wing with a Variable Camber Continuous Trailing Edge Flap Design," 32nd AIAA Applied Aerodynamics Conference, AIAA-2014-2442, June 2014.

[11]Ferrier, Y., Nguyen, N., and Ting, E., "Real-Time Adaptive Least-Squares Drag Minimization for Performance Adaptive Aeroelastic Wing," 34th AIAA Applied Aerodynamics Conference, AIAA-2016-3159, June 2016.

[12]Lebofsky, S., Ting, E., Trinh, K. V., and Nguyen, N. T., "Optimization for Load Alleviation of Truss-Braced Wing Aircraft With Variable Camber Continuous Trailing Edge Flap," 33rd AIAA Applied Aerodynamics Confererence, AIAA-2015-2723, June 2015.

[13]Nguyen, N., Ting, E., Nguyen, D., and Trinh, K., "Flight Dynamic Modeling and Stability Analysis of Flexible Wing Generic Transport Aircraft," 55th AIAA/ASME/ASCE/AHS/ASC Structures, Structural Dynamics, and Materials Conference, AIAA-2014-1040, January 2014.

[14]Tal, E. A. and Nguyen, N. T., "Unsteady Aeroservoelastic Modeling of Flexible Wing Generic Transport Aircraft with Variable Camber Continuous Trailing Edge Flap," 33rd AIAA Applied Aerodynamics Confererence, AIAA-2015-2722, June 2015.

American Institute of Aeronautics and Astronautics